Check for updates

JGR Earth Surface

RESEARCH ARTICLE
10.1029/2026JF009592

New Understanding of Complex Ice Flow in the Allan Hills Blue Ice Area From ApRES Data and Modeling

M. F. Shaya[1], T. J. Fudge[1], M. R. Koutnik[1], C. Martín[2], J. Manos[1], H. Conway[1], A. N. Horlings[3,4], and B. H. Hills[5]

[1]Department of Earth and Space Sciences, University of Washington, Seattle, WA, USA, [2]British Antarctic Survey, Cambridge, UK, [3]Institute of Arctic and Alpine Research, University of Colorado Boulder, Boulder, CO, USA, [4]Applied Physics Laboratory, University of Washington, Seattle, WA, USA, [5]Department of Geophysics, Colorado School of Mines, Golden, CO, USA

Key Points:

- We present the first englacial vertical velocity measurements from an Antarctic blue ice area, where ice up to 6 Ma has been recovered
- We identify and exclude errors from antenna positioning and compare with a simple 2-D ice-flow model that helps corroborate the data
- Most data are explained with the model, providing constraints on future modeling, but complicated near-bed signals remain

Supporting Information:

Supporting Information may be found in the online version of this article.

Correspondence to:

M. F. Shaya,
mshaya@uw.edu

Citation:

Shaya, M. F., Fudge, T. J., Koutnik, M. R., Martín, C., Manos, J., Conway, H., et al. (2026). New understanding of complex ice flow in the Allan Hills Blue Ice Area from ApRES data and modeling. *Journal of Geophysical Research: Earth Surface*, *131*, e2026JF009592. https://doi.org/10.1029/2026JF009592

Received 16 JUL 2026
Accepted 31 OCT 2026

Author Contributions:

Conceptualization: M. F. Shaya, T. J. Fudge, M. R. Koutnik
Data curation: M. F. Shaya, J. Manos
Formal analysis: M. F. Shaya, T. J. Fudge, M. R. Koutnik
Funding acquisition: T. J. Fudge, M. R. Koutnik, H. Conway
Investigation: M. F. Shaya, J. Manos, H. Conway, A. N. Horlings
Methodology: M. F. Shaya, T. J. Fudge, M. R. Koutnik, C. Martín, B. H. Hills
Software: M. F. Shaya, C. Martín
Visualization: M. F. Shaya

© 2026 The Author(s). Journal of Geophysical Research: Earth Surface published by Wiley Periodicals LLC on behalf of American Geophysical Union. This is an open access article under the terms of the Creative Commons Attribution License, which permits use, distribution and reproduction in any medium, provided the original work is properly cited.

Abstract In Antarctic blue ice areas (BIAs), wind scour and sublimation drive net ablation that, together with slow ice flow up steep bedrock topography, can preserve some of the oldest ice on Earth. Observations of englacial vertical velocities are key to understanding the past and present dynamics of BIAs and predicting their age structure. However, interpreting ice flow measurements in BIAs is challenging because of the slow (order 1 cm/yr) vertical velocities and the steep bedrock slopes. Here, we present englacial deformation profiles from 3 years of Autonomous phase-sensitive Radio Echo Sounder (ApRES) measurements along a present-day flowline at the Allan Hills, Antarctica. Through comparison across numerous measurements, we identify and exclude measurement errors, which are significant because of the very slow ice motion. The ApRES data capture (a) surface mass balance-accommodating layer thinning, (b) the vertical velocity component resulting from horizontal flow over sloping bedrock, and (c) other ice dynamic vertical velocity contributions. To understand the observations, we optimize a kinematic model that partitions ice flow between these components. With constraints from the measured bedrock topography and surface horizontal velocities, the kinematic model can fit the magnitude and shape of most vertical velocity observations both at individual sites and across the flowband. The model cannot explain some of the observed basal ice velocities, either due to amplified errors in the measurements or because of complicated dynamics, potentially including 3-D flow around bedrock obstacles and anomalous deformation in a basal unit.

Plain Language Summary Blue ice areas are regions of Antarctica where glacier ice is exposed at the surface. The Allan Hills Blue Ice Area is home to the oldest recovered ice on Earth. Measurements of the ice flow at the Allan Hills and other blue ice areas are needed to understand how old ice is preserved and to predict where else it may exist. In this paper, we use a highly precise ice-penetrating radar to measure the relative vertical velocities over the full ice thickness. The ice moves very slowly (about 1 cm/yr or less in the vertical direction); therefore, we need to account for minor errors in the measurement. The vertical velocities are complicated: at the bedrock, the ice is flowing up a subglacial mountain, whereas at the surface, the ice is affected by the gain or loss of mass. We compare the data with a simple model of ice flow, which uses measurements of the ice thickness and the surface velocities. The model can reproduce much of the data, lending confidence to the observed ice flow. Close to the bedrock, the model cannot reproduce the observations, likely because of higher errors and more complicated ice flow.

1. Introduction

Antarctic blue ice areas (BIAs) trap meteorites (Cassidy et al., 1992; Delisle & Sievers, 1991; Tollenaar et al., 2022; Zekollari et al., 2019) and archive parcels of ancient ice older than 1 Ma (Higgins et al., 2015; Y. Yan et al., 2019). While the stratigraphy of the oldest ice cores is discontinuous, the samples provide snapshots of climate conditions into the Pliocene and Miocene (Marks-Peterson et al., 2026; Shackleton et al., 2026), extending the ice core record farther back in time than traditional deep cores (EPICA community members, 2004). The oldest ice on Earth recovered to date (6 Ma in age) was located near bedrock at the Allan Hills BIA in Antarctica (Shackleton et al., 2025). In the thicker (~1,000 m) ice upstream, a proposed intermediate depth ice core is expected to contain a more continuous record that still preserves ancient ice (Kehrl et al., 2018).

The age structure of BIAs is a direct consequence of the past and present ice flow. Understanding and predicting the preservation of ancient ice therefore requires observations (e.g., Sinisalo et al., 2004; Winter et al., 2016) and

Writing – original draft: M. F. Shaya, T. J. Fudge, M. R. Koutnik
Writing – review & editing: M. F. Shaya, T. J. Fudge, M. R. Koutnik, C. Martín, J. Manos, H. Conway, A. N. Horlings, B. H. Hills

models (Grinsted et al., 2003; Kehrl et al., 2018; Zwinger et al., 2014) of BIA ice flow and ice stratigraphy. Near topographic obstructions, the ice can reach near-zero speeds that are too slow to resolve at high spatial resolution with satellite remote sensing techniques (Hui et al., 2014). Global Navigation Satellite System (GNSS) surveys of stakes embedded in the ice are used to measure surface horizontal velocities, while stake height measurements over sufficiently long time periods can measure ablation rates on the blue ice (Sinisalo et al., 2003; Spaulding et al., 2012). Repeat Autonomous phase-sensitive Radio Echo Sounder (ApRES) measurements have been used to constrain englacial vertical velocities at other ice sheet locations (e.g., Fudge et al., 2023; Hills et al., 2022; Kingslake et al., 2014). ApRES surveys of BIAs can complement other geophysical measurements and offer insight into the deformation across the ice column.

In this study, we present the first interferometric ApRES survey of the Allan Hills BIA, where the National Science Foundation Center for Oldest Ice Exploration (NSF COLDEX) supported 4 years of ground-based geophysical measurements in addition to extensive ice core drilling. The vertical velocities are on the order of 1 cm/yr, meaning minor errors that could be neglected at most sites are large relative to the signal. We use a wealth of data, including multiple years and antenna polarizations, to evaluate the velocities and to remove apparent velocity signals that are attributable to small inconsistencies in the radar setup between years.

To investigate the ice flow signals in the ApRES data, we compare the observed velocities with a kinematic model. The model describes velocities without considering stresses based on the ground penetrating radar-observed surface and bedrock geometry (Conway & Campbell, 2017), surface horizontal velocities observed with GNSS stake measurements (Shaya, Manos, Banerjee, et al., 2026; Spaulding et al., 2012), and tuneable velocity shape functions. Because of the strong data constraints, model agreement with the observations supports the integrity of the data and can offer insights into the different vertical velocity components captured by the ApRES measurement. The new observations of englacial velocities represent an advance in characterizing ice flow at the region with the oldest known ice on Earth.

1.1. Past Research at the Allan Hills

The Allan Hills BIA is located near the margin of the East Antarctic Ice Sheet and next to a wishbone shaped nunatak (an exposed mountaintop jutting out from surrounding ice) in the Transantarctic mountains. The bare ice fields near the Allan Hills first became known as meteorite stranding sites (Cassidy et al., 1992; Harvey, 2003), preserving meteorites with terrestrial ages up to 1.54 Ma (Fireman et al., 1979) and 2 Ma (Scherer et al., 1997). The recovery of ancient meteorites led Whillans and Cassidy (1983) to posit that the Allan Hills ice fields might also contain ancient ice core records. Shallow ice coring expeditions subsequently recovered a continuous core dated to ∼90–250 ka (Spaulding et al., 2013), as well as shallow discontinuous records going back 1 Ma (Higgins et al., 2015), 2.7 Ma (Y. Yan et al., 2019), and most recently 4.6 Ma (Marks-Peterson et al., 2026) and 6 Ma (Shackleton et al., 2025).

Ice at the Allan Hills flows approximately grid south (Figure 1) from a local ice divide (Schultz et al., 1990), with the fastest flow along a deeper channel that separates the Allan Hills ice field from the nearby North-West ice field (Delisle & Sievers, 1991). Closer to the nunatak, the basal topography is more pronounced (Brook & Nesbitt, 2023), the ice flow becomes strongly compressive, and surface horizontal velocities approach zero (Spaulding et al., 2012). Wind-driven ablation of the exposed blue ice balances much of the ice flux, while some ice can flow overtop the topographic barriers (Cassidy et al., 1992). The region's ice flow stability on glacial-interglacial timescales is not well constrained: Atkins et al. (2002) describe erosional features in the center of the Allan Hills nunatak which suggest the ice stand was once ∼100 m higher than the present limit, while Coren et al. (2003) suggest that present-day ice rises in the region must be a transient feature indicating higher ice in the past.

Past modeling of velocities and age structure at the Allan Hills applied a kinematic flowline model (Grinsted et al., 2003) constrained by surface velocities and sparse surface mass balance (SMB) rates (Spaulding et al., 2012). By comparing the modeled layers to the 7 MHz ground penetrating radar profiles of the bedrock topography and englacial layers (Conway & Campbell, 2017), Kehrl et al. (2018) find that an intermediate depth (∼1,000 m) ice core site in the snow-covered region up-flow from shallow coring locations may contain a 1 Ma continuous ice core record. The measurements of vertical velocities presented in this paper lie along the radar profiles used in past modeling. These new data help illuminate complex ice flow dynamics and can be used in the future to improve depth-age modeling.

21699011, 2026, 11, Downloaded from https://agupubs.onlinelibrary.wiley.com/doi/10.1029/2026JF009592 by British Antarctic Survey, Wiley Online Library on [27/11/2026]. See the Terms and Conditions (https://onlinelibrary.wiley.com/terms-and-conditions) on Wiley Online Library for rules of use; OA articles are governed by the applicable Creative Commons License

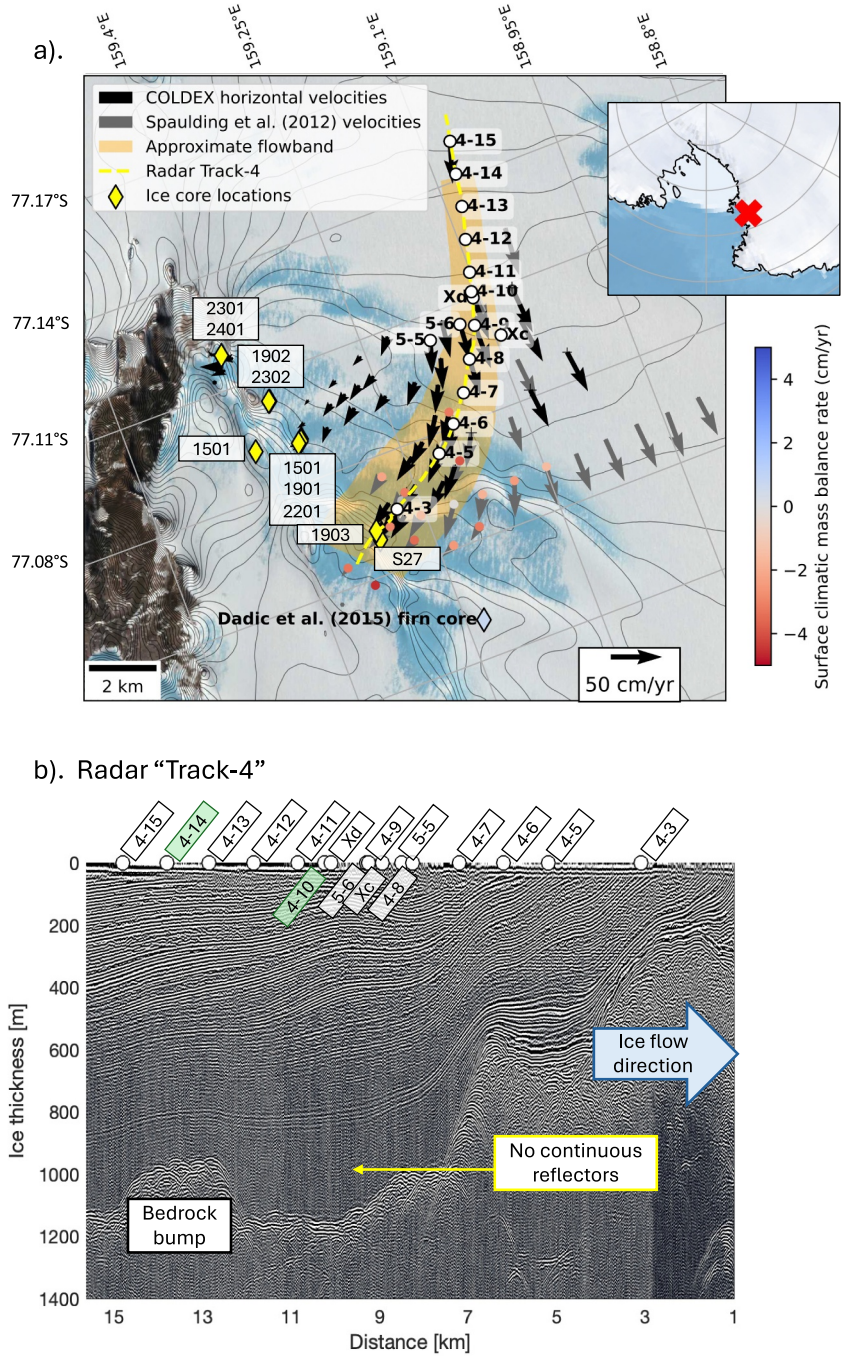

Figure 1. (a) Map of the Allan Hills region including surface velocities (black and gray arrows, Shaya, Manos, Banerjee, et al., 2026; Spaulding et al., 2012), the profiling radar track 4 (yellow dashed line), an approximate flowband width (orange shaded region), and ice core sites (yellow diamonds, Higgins et al., 2015; Kirkpatrick et al., 2025; Y. Yan et al., 2019). Autonomous phase-sensitive Radio Echo Sounder (ApRES) measurement sites are marked with white dots. Also plotted are surface mass balance constraints from ablation stakes (Spaulding et al., 2012) and a firn core (Dadic et al., 2015). (b) The 7 MHz mono-pulse radar reveals internal layers and the bed along track 4 (Conway & Campbell, 2017). ApRES site locations are indicated with the white dots at the surface; the site locations highlighted with green boxes are featured in Figures 2 and 8.

1.2. Structure of the Paper

This paper presents a novel data set of vertical velocity measurements from the slow-flowing Allan Hills Blue Ice Area in Antarctica, and interprets these data using a kinematic model constrained by surface velocities and

21699011, 2026, 11, Downloaded from https://agupubs.onlinelibrary.wiley.com/doi/10.1029/2026JF009592 by British Antarctic Survey, Wiley Online Library on [27/11/2026]. See the Terms and Conditions (https://onlinelibrary.wiley.com/terms-and-conditions) on Wiley Online Library for rules of use; OA articles are governed by the applicable Creative Commons License

21699011, 2026, 11, Downloaded from https://agupubs.onlinelibrary.wiley.com/doi/10.1029/2026JF009592 by British Antarctic Survey, Wiley Online Library on [27/11/2026]. See the Terms and Conditions (https://onlinelibrary.wiley.com/terms-and-conditions) on Wiley Online Library for rules of use; OA articles are governed by the applicable Creative Commons License

flowband geometry. The paper's organization represents a departure from the standard methods/results structure, because the ideas and intuition developed in each step of the analysis help support the next. The three analysis sections involve: (a) processing and evaluation of the ApRES data to isolate the most reliable signals, (b) individual-site model-data comparisons that corroborate the data and partition between different contributions to the vertical velocities, and (c) a flowband model optimization against the data. Below, we expand on the contributions of each section.

In Section 2, we describe the ApRES data collection and processing to resolve the very slow vertical velocities of the Allan Hills BIA. Using 3 years of repeat measurements to assess the reliability of the ApRES signals, we identify and exclude apparent velocity signals caused by small variations in the antenna setup between years. We also discuss the Lagrangian frame of the ApRES measurements. Because ApRES measurements repeatedly sample the same parcel of ice as it flows, they capture both the vertical motion driven by SMB and other dynamics, which we refer to as the 1-D vertical velocity component, and the vertical velocities induced by horizontal flow over sloping bed topography.

In Section 3, we compare the individual-site ApRES data to a kinematic model that is constrained by measured surface velocities and flowline geometry. Because the model partitions vertical velocities between SMB-accommodating, topography-driven, and ice dynamic flow, it is a useful tool for understanding and corroborating ApRES observations. We show that some of the strain-rate reversals with depth are consistent with expectations for ice flow over the steep bedrock topography of the Allan Hills. However, some of the signals within the data—especially near the bed—cannot be explained with our model, whether due to measurement errors in the deepest ice or complicated basal ice flow that exceeds model capabilities. In anticipation of the following section, we create a curated data set of the most robust velocities, excluding anomalous basal signals that cannot be corroborated by the kinematic model.

In Section 4, we conduct a flowband model optimization, which solves for the Lliboutry (1979) ice flow parameter $p(x)$ and the SMB across all sites at once to account for the interdependence of ice dynamic properties at the neighboring ($\sim$1 km spacing) ApRES sites. We restrict analysis to the curated data set. While this may exclude some real velocity signals, it enables a model representation of the well-behaved parts of the flow field and allows for investigation of ice dynamic changes across the flowband. Additionally, we assess model assumptions by introducing a surface velocity-constrained flowband width term and then calculating the SMB rates needed to preserve ice mass continuity across the flowband.

In Section 5, we discuss implications of the model-data comparisons at the Allan Hills and offer considerations for future ApRES surveys of BIAs. The individual-site model fits show that the data contains strong topographic-driven vertical velocity components. The flowband model fits demonstrate that the ApRES survey captures reasonable changes to the deformation along flow. Model-data mismatches can indicate 3-D flow around bedrock obstacles or other complicated basal ice signals, which may be significant toward predicting the age structure and stratigraphic continuity of a proposed intermediate depth ice core site in the region.

2. ApRES Data and Methods

ApRES instruments measure the amplitude and phase of reflected electromagnetic waves, enabling mm-scale measurement precision (Brennan et al., 2014; Nicholls et al., 2015). Repeat ApRES acquisitions can track the relative motion of internal ice reflectors. On ice shelves and icebergs, repeat ApRES is used to observe basal melt rates (e.g., Corr et al., 2002; Marsh et al., 2016; Schild et al., 2024; Vaňková et al., 2020; Wild et al., 2024; Zeising et al., 2022). On ice sheets, repeat ApRES can measure englacial relative vertical velocities and vertical strain rates at ice divides (Chung et al., 2023; Fudge et al., 2023; Kingslake et al., 2014, 2016) and flank sites (Hills et al., 2022).

In Sections 2.1 and 2.2 we describe the data collection and processing for the ApRES survey of the Allan Hills. Resolving vertical velocities at the Allan Hills is difficult because of the very low strain rates (order of 10^{-5} yr^{-1}); however, our repeat measurements from 3 years and multiple polarizations provide a wealth of data with which to evaluate the ApRES signal. In Section 2.3 we show that diverging relative vertical velocities in the top 200 m, including an apparent firn extension signal, can be attributed to small changes in the antenna separation between measurements. In Section 2.4 we demonstrate that periodic signals in some of the profiles are consistent with modeled effects of $<5°$ offsets in the antenna rotation angle between measurements. Finally, in Section 2.5 we

discuss the measurement framework of the ApRES in anticipation of comparing the data with a model of vertical velocities over depth.

2.1. ApRES Data Collection

We present data from 16 sites, which span snow-covered and ice-covered areas of the Allan Hills, with ice thicknesses ranging from 300 to 1,200 m (Figure 1). Most sites lie along what we refer to as "track 4": an approximate flowline measured with 7 MHz ground penetrating radar (Conway & Campbell, 2017). The ApRES site naming convention includes the radar track name and the approximate distance along-track (e.g., site "4-10" for 10 km along track 4). Ice flow at the Allan Hills is additionally characterized by GNSS stake measurements of horizontal velocities (Shaya, Manos, Banerjee, et al., 2026; Spaulding et al., 2012), ablation stake surveys (over ∼14 years, Spaulding et al., 2012), and an accumulation rate estimate from the ^{210}Pb activity in a firn core (Dadic et al., 2015).

Each ApRES site was surveyed in the 2022–23, 2023–24, and 2024–25 field seasons (hereafter years 1–3). In each field season, we collected ∼15 min acquisitions (about ten 100 s bursts) in two co-polarized and at least one cross-polarized configuration (Figure 2d). Settings were the same across all measurements with attenuation set to 20 dB and gain set to −4 dB. The antennas were spaced approximately 8 m apart by extending the cables their full length. Each antenna was marked with one flag to enable repeat measurements. The radar setup ran roughly parallel to ice flow, with the transmitting (Tx) antenna down-flow (see Figure 2d). We aligned the antenna in either the "H" or "V" position by sighting down the center toward the opposite antenna. Minor inconsistencies in the setup between years are to be expected.

2.2. ApRES Data Processing

ApRES acquisitions were processed following Brennan et al. (2014). For each measurement, we filtered the data by removing chirps where the mean correlation to the average chirp (across all bursts) was less than 0.95 in the top 200 m of the profile (see Figure S2 in Supporting Information S1), then we averaged the remaining chirps. Figures 2a, 2e, and 2h show the power return from the year 1 co-polarized (HH, VV) ApRES acquisitions at sites 4-14, 4-10, and 4-7. The signal-to-noise ratios enable resolution of velocities all the way to the bed.

We compute relative vertical velocity profiles for pairs of acquisitions separated in time by 1 or 2 years using standard ApRES interferometric processing (Hills et al., 2022; Kingslake et al., 2014). We co-register the data in depth, finding the range bin offsets over depth that yield the highest correlation between the two measurements. Because velocities at the Allan Hills are small relative to the ApRES range bins of 0.21 m, we do not report calculated velocities at depths where the offset of co-registration is different from the mode. We calculate the phase shift between the two depth-aligned measurements using an 80 m moving window. Assuming a constant electromagnetic propagation in ice, the unwrapped phase shift corresponds to a distance shift for the internal reflectors: this distance over the measurement interval time is the relative vertical velocity profile. Vertical velocities are only used in the analysis when the correlation exceeds a threshold of 0.5. Error bars are calculated by a noise phasor approach (Kingslake et al., 2014) that estimates uncertainty in the phase from the reflection signal-to-noise ratio (SNR).

The colored lines in Figures 2b, 2f, and 2i show the relative vertical velocities calculated from all polarizations and all years (year 1–2, 1–3, 2–3). We align all profiles such that the mean from 200 to 500 m depth is zero. In theory, absolute vertical velocities can be calculated by referencing the profiles to a fixed datum, often chosen to be the basal or surface velocity (Fudge et al., 2023); however, we choose to keep the profiles in relative vertical velocity space. Due to gaps in the relative velocity profile near the bed where correlations are below 0.5, aligning to a fixed bed would require extrapolating basal velocities, which is challenging given the large uncertainties (low SNRs) of the near bed data. Aligning to a known surface velocity is not feasible, because observing cm-scale SMB or surface vertical velocities is challenging: at many of the ApRES sites, existing GNSS data do not even constrain the sign of the surface vertical velocity.

We compute a combined profile for each site using a weighted-slope approach, as shown in Figures 2c, 2g, and 2j. The slopes of each profile are calculated using a linear regression over a moving window of 40 data points. The black error bars represent the integral of the average line slopes, weighted by the noise phasor uncertainties. This approach was constructed to average over the shape of the relative vertical velocity profiles—that is, the strain

21699011, 2026, 11, Downloaded from https://agupubs.onlinelibrary.wiley.com/doi/10.1029/2026JF009592 by British Antarctic Survey, Wiley Online Library on [27/11/2026]. See the Terms and Conditions (https://onlinelibrary.wiley.com/terms-and-conditions) on Wiley Online Library for rules of use; OA articles are governed by the applicable Creative Commons License

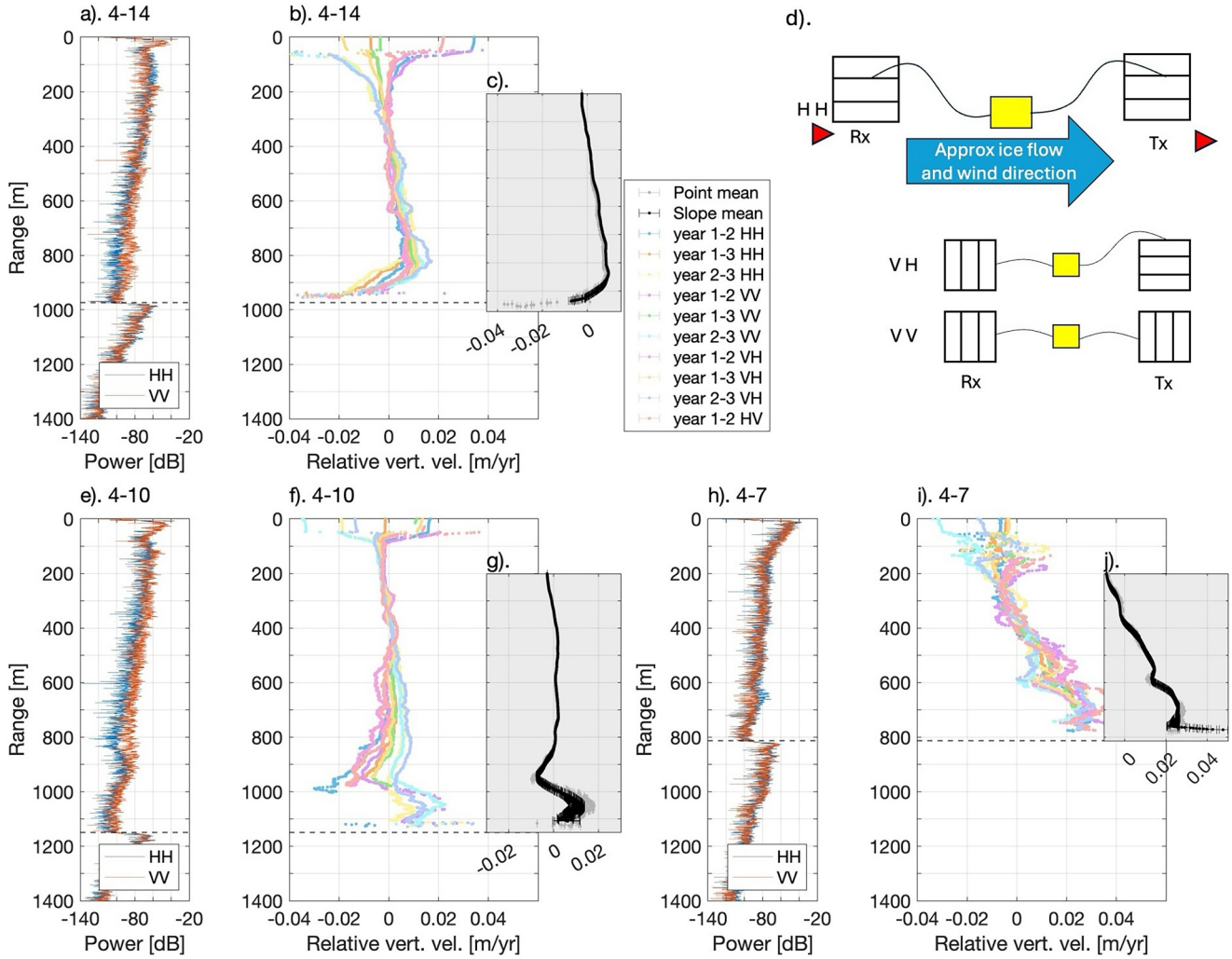

Figure 2. Example Autonomous phase-sensitive Radio Echo Sounder (ApRES) data and relative vertical velocities. (a, e, h). Power return (dBs) from the year 1 sites 4-14, 4-10, and 4-7 HH (blue) and VV (orange) measurements. (b, f, i) Relative vertical velocity measurements from sites 4-14, 4-10, and 4-7. The colored lines represent individual measurements using different polarizations and different combinations of years (year 1–2, 1–3, 2–3). All profiles have been shifted so the mean over 200–500 m depth is zero. (c, g, j). Average vertical velocity profiles from 4-14, 4-10, and 4-7. The black error bars are calculated by averaging velocity slopes; the gray error bars represent point averages of the individual velocity profiles. (d). Diagram of the ApRES measurement setup with antenna orientations for the Rx (receiving) and Tx (transmitting) antennas in different polarizations (HH, VH, VV).

rate—and does not require assuming a reference velocity to align the curves. For comparison, we also plot the weighted point average (gray error bars), which have a similar shape but are more sensitive to outlier points.

2.3. Effects of Variable Antenna Spacing

The relative vertical velocities computed using different polarizations and different combinations of years diverge sharply in the top 200 m depth (Figure 3). Across all sites, velocities computed using data from years 1–2 indicate near-surface extension (lines curving to the right), while velocities computed from years 2–3 indicate near-surface compression. While the very near-surface (top ∼10 m) blue ice may experience transient extension and compression from thermal changes (Lombardi et al., 2019), the observed velocity differences extend far deeper than the seasonal thermal signal. Here, we propose that the diverging near-surface velocity signals result from systematic variations in the ApRES antenna spacing across different years.

As shown in common midpoint applications, changing the antenna separation distance results in changes to the path length (Arthern et al., 2013, Text S2.1 in Supporting Information S1); the resulting phase difference manifests as an apparent velocity signal. Moving the antennas closer together shortens the radar path length and

21699011, 2026, 11, Downloaded from https://agupubs.onlinelibrary.wiley.com/doi/10.1029/2026JF009592 by British Antarctic Survey, Wiley Online Library on [27/11/2026]. See the Terms and Conditions (https://onlinelibrary.wiley.com/terms-and-conditions) on Wiley Online Library for rules of use; OA articles are governed by the applicable Creative Commons License

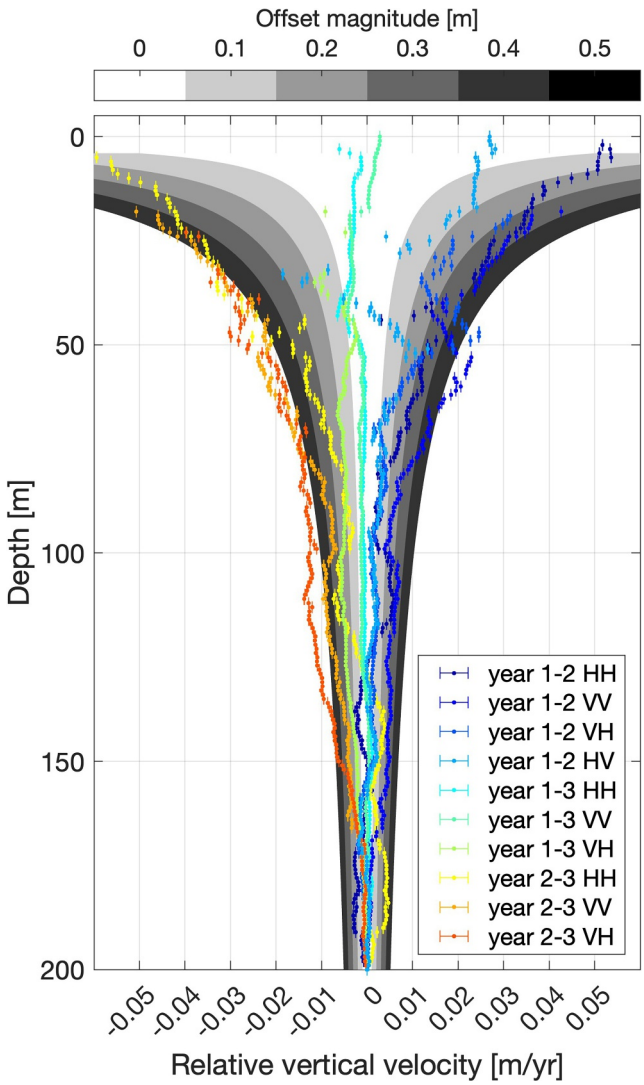

Figure 3. Antenna spacing changes complicate the near-surface data. The colored lines show individual relative vertical velocity profiles in the top 200 m at site 4-14. To resolve the near-surface signal, these velocities are calculated with a 20 m moving window. Year 1–2 velocities show apparent, though unphysical, near-surface vertical extension; year 2–3 velocities show strong near-surface compression. The shaded gray lines demonstrate the modeled apparent vertical velocities for different magnitude offsets in the antenna spacing between acquisitions.

results in an apparent firn extension signal. Moving the antennas farther apart has the opposite effect. For deeper reflectors, the wave path approaches a vertical line, and the effect of horizontal antenna spacing offsets is reduced (see Figure 3).

Because deformation rates at the Allan Hills are slow, small antenna spacing changes in our survey preclude robust measurements in the near-surface. The near-surface signal may also be complicated by the antenna radiation pattern in the top 20 m (T. J. Young, Schroeder, et al., 2021) and the changing density of the firn at sites where a firn column is present. In the combination profiles (see Section 2.2) and all further analysis, we exclude the top 200 m of the interferometric velocities.

2.4. Effects of Variable Antenna Rotation

Oscillatory effects appear in some of the individual ApRES profiles across all depths (see Figures 4a–4c). We interpret these signals to result from small changes to the antenna rotation between measurements in a region where the bulk alignment of ice crystal *c*-axes, termed the ice fabric, has a strong horizontal asymmetry (see Figure S5, Text S2.2 in Supporting Information S1).

Polarimetric phase-sensitive radar is commonly used to measure the horizontal ice fabric asymmetry (Hills et al., 2025; Jordan et al., 2019; T. J. Young, Martín, et al., 2021; Zeising et al., 2023). These approaches use orthogonally polarized radar acquisitions. However, in a region of strong fabric, azimuthal offsets of less than 5° can result in phase offsets that create apparent vertical velocities.

Following Ershadi et al. (2022); Fujita et al. (2006), we model the phase of initially linearly polarized electromagnetic waves passing through a fabric with a prescribed depth-variable horizontal asymmetry, ΔE (Figure 5a). The model assumes isotropic scattering and neglects attenuation, which would reduce the power in the deepest ice but would not affect the phase. Figures 5c and 5d show the phase offsets, corresponding to apparent velocities over 1 year, that result from rotating the antennas 0–10° relative to (5c) zero degrees azimuth with respect to the girdle fabric and (5d) 45° azimuth. The periodicity of the phase offset depends on the horizontal asymmetry ΔE. The amplitude of the phase offset depends on both the rotation offset angle and the antenna azimuth relative to the fabric (see schematic, Figure 4d). When the transmit polarization is aligned with the fabric axes, the effect of rotational offsets is smallest and most sinusoidal. As the antenna azimuth nears 45° relative to the fabric, the amplitude increases nonlinearly and the phase offsets over depth become skewed (Figure 5b).

Antenna rotation offset effects can explain the oscillating signals in the ApRES profiles. Figures 4a–4c compare select interferometric profiles (colored lines) with modeled apparent velocities from antenna rotation effects superimposed on the background ApRES signal (black dashed lines). The model can achieve the periodicity and amplitude of the data signals with rotation offsets under ±5° and girdle strengths in the range $\Delta E = 0.3–0.5$. At the Allan Hills, antenna rotation effects are significant due to both the strong horizontal fabric asymmetry and the slow background velocity signal.

We do not see any systematic patterns in the oscillatory signals across polarizations or years, suggesting that antenna rotation offsets were small and random. In all further analysis, we use the weighted slope combination profile, which captures the trends that are robust across all the data. At sites where the number of ApRES profiles is limited by noisy acquisitions (4-12, 4-11, 4-6), the combined profiles may retain effects of antenna rotation offsets.

21699011, 2026, 11, Downloaded from https://agupubs.onlinelibrary.wiley.com/doi/10.1029/2026JF009592 by British Antarctic Survey, Wiley Online Library on [27/11/2026]. See the Terms and Conditions (https://onlinelibrary.wiley.com/terms-and-conditions) on Wiley Online Library for rules of use; OA articles are governed by the applicable Creative Commons License

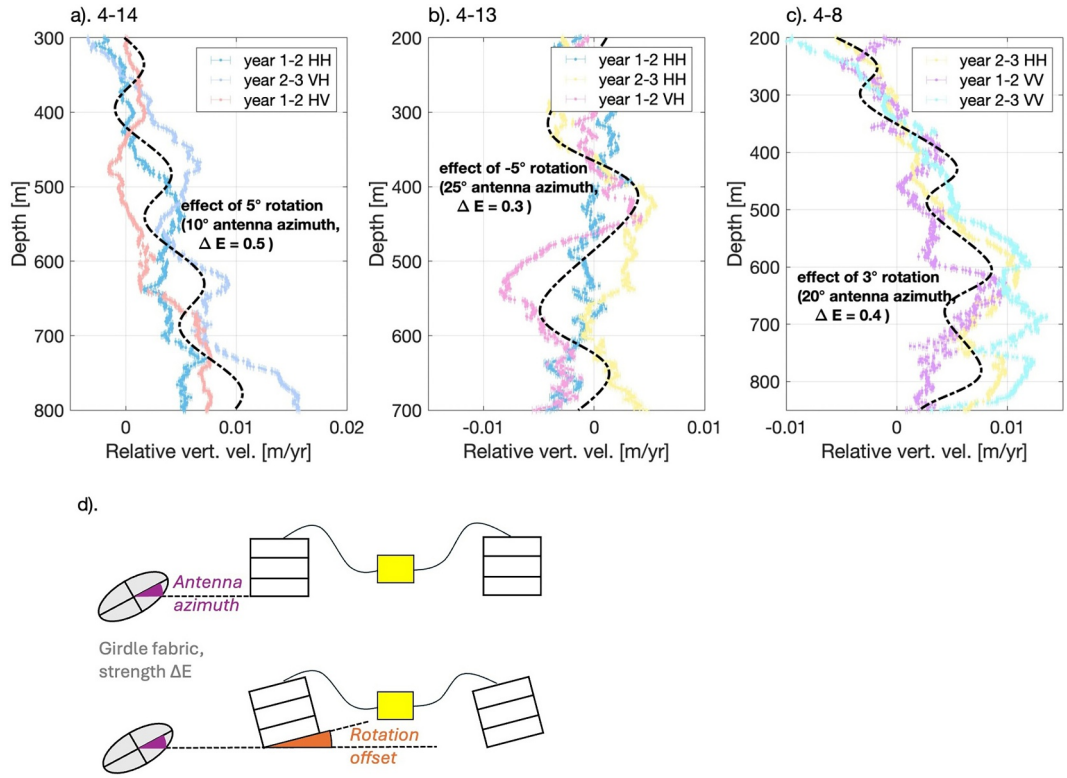

Figure 4. Oscillatory apparent velocity signals attributed to changes to the antenna rotation. (a–c). Select vertical velocity profiles at mid depths from sites 4-14 (a), 4-13 (b), and 4-8 (c) showing periodic fluctuations that we attribute to antenna rotation effects. The dashed lines represent modeled apparent velocities over 1 year for a given rotation offset ($5°, -5°, 3°$), antenna azimuth ($10°, 25°, 20°$) and horizontal fabric asymmetry ($\Delta E = 0.5, 0.3, 0.4$). For better comparison with the data, the modeled velocities are superimposed on a quadratic fit to the ApRES data within the plotted depth range. (d). Diagram of antenna rotation offsets.

2.5. ApRES Measurement Frame

ApRES measurements operate mostly within a Lagrangian frame, because the antenna locations, marked by flags, move horizontally with the surface ice flow. As a result, ApRES interferometric measurements capture both: (a) the compression or extension of englacial layers due to SMB and other ice dynamic processes and (b) the component of vertical velocity resulting from horizontal flow over a sloping bed (Holschuh et al., 2017; Summers et al., 2021). We refer to these contributions as the 1-D and topography-driven vertical velocity components (Figure 6). At the Allan Hills, steep bedrock slopes and low SMB rates that range from about −5 to +3 cm/yr mean that the topography-driven component of vertical velocities is a large part of the ApRES signal.

The measurement framework is more complicated near the bed and in regions of steep layering. In a shear-driven regime, differential velocities between the surface and the basal ice can introduce an offset in repeat measurements between the radar and the ice parcels that the radar is sensing, leading to Lagrangian errors in the velocity calculations (Hills et al., 2022). In addition, off-nadir reflections from steeply dipping layers (e.g., Kirkpatrick et al., 2025) introduce uncertainty both in the range to depth conversion and in the direction of ice motion being resolved. These measurement errors may complicate the basal ApRES signals, as discussed in Section 5.3.

3. Individual Site Modeled and Measured Velocities

To understand the different ice flow components resolved in the ApRES interferometry, we compare the data with a kinematic model adapted from Waddington et al. (2007). We present the model in Section 3.1. The model uses observed surface horizontal velocities and ice thicknesses, which strongly constrain the topography-driven vertical velocity component. In Section 3.2, we fit velocities at individual ApRES sites using data constraints (Conway & Campbell, 2017; Shaya, Manos, Banerjee, et al., 2026; Spaulding et al., 2012) and an optimization for

21699011, 2026, 11, Downloaded from https://agupubs.onlinelibrary.wiley.com/doi/10.1029/2026JF009592 by British Antarctic Survey, Wiley Online Library on [27/11/2026]. See the Terms and Conditions (https://onlinelibrary.wiley.com/terms-and-conditions) on Wiley Online Library for rules of use; OA articles are governed by the applicable Creative Commons License

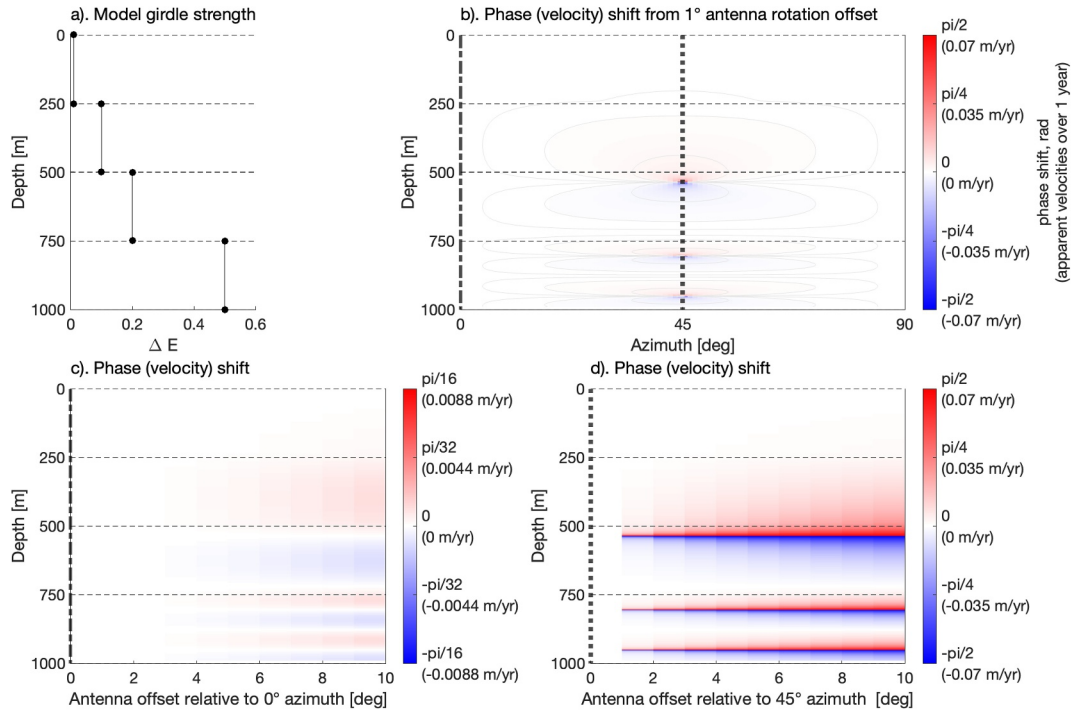

Figure 5. Modeled apparent velocities resulting from antenna rotation offsets. (a) Prescribed horizontal fabric asymmetry ΔE over depth. (b) Modeled phase shift (apparent velocity over 1 year) over depth and initial antenna azimuth for two polarimetric radar measurements with a 1° offset in antenna rotation. The strength of the effect depends strongly on the initial radar azimuth relative to the fabric. (c) Modeled phase shifts (apparent velocities) resulting from 1 to 10° rotation offsets from the 0° fabric-relative antenna azimuth. (d) Same as (c), except the rotation offsets are away from the 45° fabric-relative antenna azimuth. Note the 8-fold increase in the velocity colorbar scale.

model free parameters. We discuss the resulting model-data fits in Section 3.3. Much of the ApRES data is consistent with kinematic model representations, including some strain-rate reversals over depth. Finally, in Section 3.4, we create a curated data set that represents the most robust relative vertical velocity measurements, which will be used in Section 4 to analyze the ice dynamic component of flow across track 4.

3.1. Kinematic Model of Vertical Velocities

Following Waddington et al. (2007), we define the kinematic model horizontal and vertical velocities over the along-flow dimension x as:

$$u(x,\hat{z}) = \phi(x,\hat{z})\,\overline{u}(x) \tag{1}$$

$$w(x,\hat{z}) = \underbrace{-\dot{b}\psi(x,\hat{z})}_{\text{term 1: SMB-accommodating}} + \underbrace{\overline{u}\phi(x,\hat{z})\left(\frac{\partial B}{\partial x} + \hat{z}\frac{\partial H}{\partial x}\right)}_{\text{term 2: topography-driven}} - \underbrace{\overline{u}H\int_0^{\zeta}\frac{\partial\phi(x,\zeta)}{\partial x}\,d\zeta}_{\text{term 3: ice dynamic}} \tag{2}$$

where $\overline{u}(x)$ is the mean horizontal ice flow, $\dot{b}$ is the SMB rate, $B(x)$ is the bed depth, $S(x)$ is the surface elevation, $H(x) = S(x) - B(x)$ is the ice thickness, and $\hat{z} = \frac{z - B(x)}{H(x)}$ is a normalized depth coordinate. Waddington et al. (2007) additionally consider basal melting and a changing surface elevation, which we neglect here. The functions $\phi(x,\hat{z})$ and $\psi(x,\hat{z})$ are velocity shape functions with $\psi(x,\hat{z}) = \int_0^{\hat{z}}\phi(x,\zeta)\,d\zeta$. The three terms in the equation for $w(x,\hat{z})$ represent (a) SMB-accommodating velocities, (b) topography-driven vertical velocities, which are parallel to the bed at the bed and parallel to the surface at the surface, and (c) ice dynamic velocities resulting from longitudinal changes in the shape of the horizontal velocities (Fudge et al., 2023).

21699011, 2026, 11, Downloaded from https://agupubs.onlinelibrary.wiley.com/doi/10.1029/2026JF009592 by British Antarctic Survey, Wiley Online Library on [27/11/2026]. See the Terms and Conditions (https://onlinelibrary.wiley.com/terms-and-conditions) on Wiley Online Library for rules of use; OA articles are governed by the applicable Creative Commons License

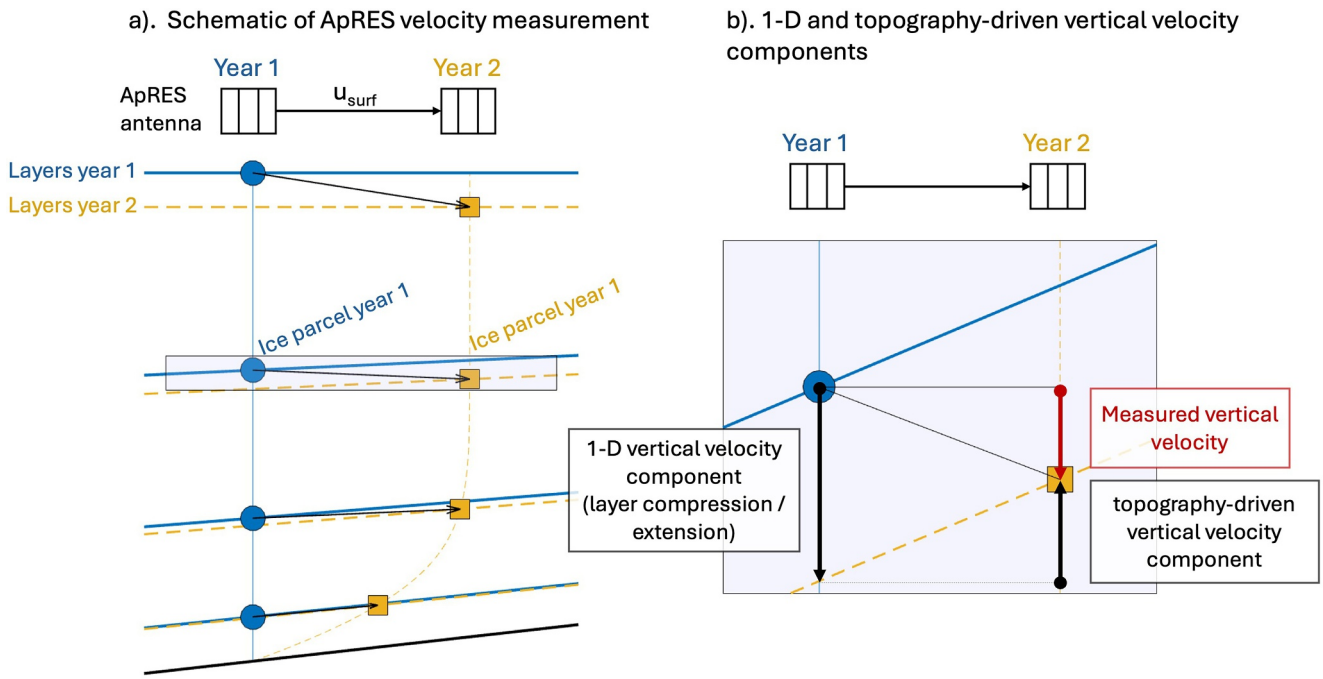

Figure 6. Diagram showing the 1-D and topography-driven vertical velocity components resolved in the ApRES interferometric measurements. (a) Schematic of layers and ice parcels in year 1 (solid layers, blue dots) and year 2 (dashed layers, yellow boxes). The ApRES setup (white antennae) moves horizontally with the surface ice flow. The ice parcels move due to surface mass balance and ice dynamic effects; they also move upward due to horizontal flow over the sloping bedrock. Near the bed, Lagrangian effects introduce an offset between the moving antenna and the stationary ice parcels. (b) Components of vertical velocities in the ApRES measurement. The 1-D vertical velocity component represents the movement of layers at a fixed horizontal position. The topography-driven vertical velocity component (also termed a layer-following velocity) represents the vertical velocities induced by horizontal flow over sloping bedrock. The ApRES measures the sum of these two vertical velocity components.

The shape function $\phi(x, \hat{z})$ defines how the horizontal velocity profile changes over depth and along flow. Because we assume a frozen bedrock interface, the velocities are always zero at the bed. We follow Chung et al. (2025), Fudge et al. (2023), Parrenin and Hindmarsh (2007) in using the simple and versatile Lliboutry (1979) formulation, which can be tuned against observations using the parameter $p(x)$ (Figure 7a). A high p value (e.g., 20) concentrates horizontal deformation near the bed, consistent with easier deformation due to warmer temperatures or highly developed fabric at depth whereas a low p value (e.g., 0.1) distributes strain more evenly throughout the ice column, consistent with flow at a divide (Raymond, 1983).

3.2. Fitting the Model to Individual-Site Velocities

To understand which parts of the ApRES profiles are consistent with the kinematic model and which components of velocity are captured in the data, we optimize model free parameters to fit the data. We minimize the objective function:

$$\sum_{\hat{z}} (w(\hat{z}_i) - \mathcal{W}(\hat{z}_i) - a)^2 \tag{3}$$

for model velocities $w(\hat{z})$ and ApRES data $\mathcal{W}(\hat{z})$. The parameter a represents a depth-constant offset in the $[-0.2, 0.2]$ m/yr range, which allows the relative vertical velocity data to adjust by one ApRES range bin. The offset a accounts for the fact that the ApRES are not referenced to an absolute datum due to the complicated near-bed signals and the difficulties of observing cm-scale surface vertical velocities.

The model velocities w depend on the ice thickness H and its gradient $\frac{dH}{dx}$, the surface gradient $\frac{dS}{dx}$, the surface horizontal ice velocity, the SMB rate $\dot{b}$, and the value of p and its gradient $\frac{dp}{dx}$. Because the ApRES sites are either on or near track 4, we use the surface elevation $S(x)$ and ice thickness $H(x)$ from the 7 MHz profiling radar (Conway & Campbell, 2017); both the surface and thickness are smoothed using a Gaussian filter with a 1,000 m

21699011, 2026, 11, Downloaded from https://agupubs.onlinelibrary.wiley.com/doi/10.1029/2026JF009592 by British Antarctic Survey, Wiley Online Library on [27/11/2026]. See the Terms and Conditions (https://onlinelibrary.wiley.com/terms-and-conditions) on Wiley Online Library for rules of use; OA articles are governed by the applicable Creative Commons License

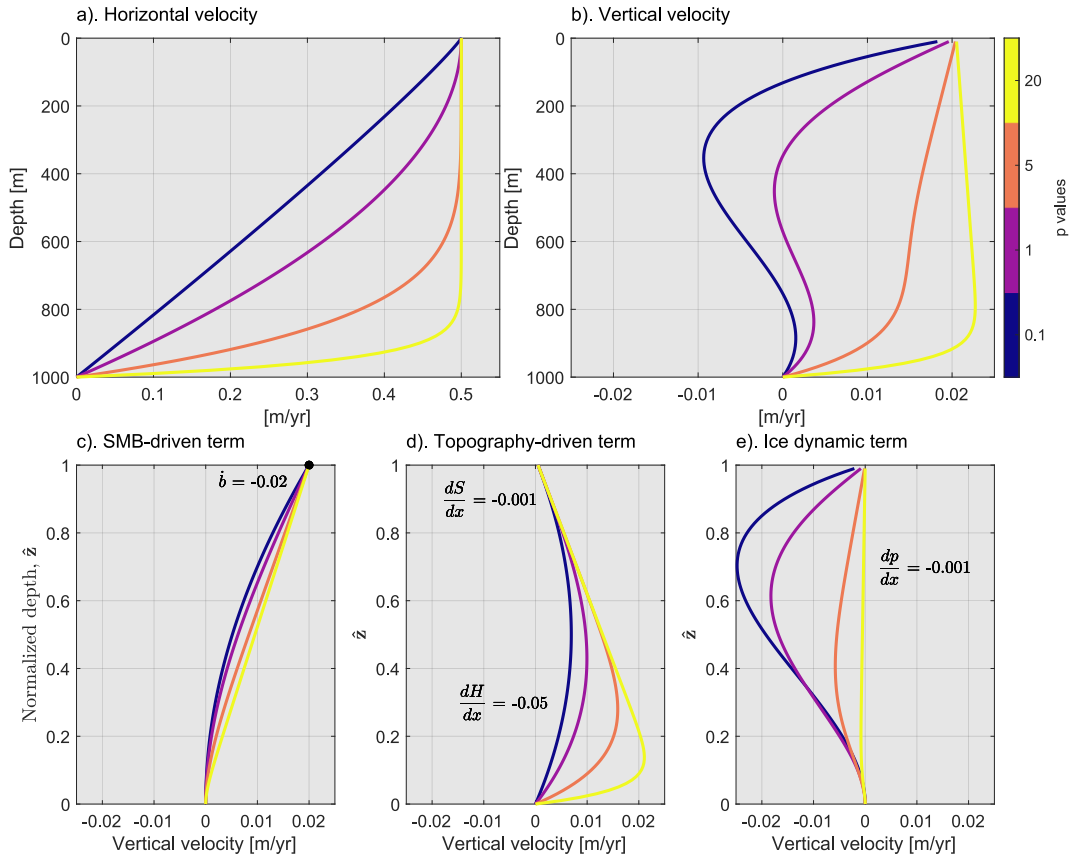

Figure 7. Model horizontal and vertical velocities for different values of p and fixed $\dot{b}$, $\frac{dH}{dx}$, $\frac{dp}{dx}$. (a) Lliboutry shape function horizontal velocities with 0.5 m/yr surface velocity. Higher values of p (bright yellow) concentrate the deformation near the bed, while low values of p (dark purple) result in a more linear profile. (b) Modeled vertical velocities for different values of p, with components shown in (c–e). (c) Surface mass balance-accommodating vertical velocity term with an ablation rate of $\dot{b} = -0.02$ m/yr. (d) Topography-driven vertical velocity term with upward-sloping bedrock (decreasing ice thickness, with $\frac{dH}{dx} = -0.05$) and a downward surface slope ($\frac{dS}{dx} = -0.001$). (e) Ice dynamic vertical velocity term with $\frac{dp}{dx} = -0.001$.

window (approximately one ice thickness) to capture variability on scales relevant for ice flow (Figure 8d). We interpolate the surface horizontal velocity u_{surf} along track 4 using a distance-weighted least squares fit to the GNSS stake measurements (Figure 8c).

The remaining parameters $\left(\dot{b}, p, \frac{dp}{dx}\right)$ are tuned in the optimization. Based on the sparse accumulation and ablation constraints (Dadic et al., 2015; Spaulding et al., 2012), we limit $\dot{b}$ to the range $[-0.05, 0.03]$. We let p vary between 0.1 and 20, which allows a broad set of horizontal shape function velocities (Figure 7). In some model fits we turn off the ice dynamic term by setting $\frac{dp}{dx}$ to zero. In other model fits that include the ice dynamic term, we optimize the parameter $\frac{1}{p}\frac{dp}{dx}$ within the bounds $[-0.0005, 0.0005]$; these bounds were chosen such that the term is the same order of magnitude as the SMB-accommodating and topography-driven velocity components. Optimizing for $\frac{1}{p}\frac{dp}{dx}$ accounts for the nonlinearity of the ice dynamic term with p; equivalently, the optimization is for the parameter $\frac{dq}{dx}$ in the range $[-0.0005, 0.0005]$ where $q = \log p$.

We solve for parameters using the MATLAB function `fmincon` which identifies local minima of constrained nonlinear multivariate problems using a gradient descent method (Pettit et al., 2014). The goal of the individual site optimizations is to understand whether and how the ApRES data are consistent with a kinematic model representation, therefore we choose not to explore all possible local minima.

21699011, 2026, 11, Downloaded from https://agupubs.onlinelibrary.wiley.com/doi/10.1029/2026JF009592 by British Antarctic Survey, Wiley Online Library on [27/11/2026]. See the Terms and Conditions (https://onlinelibrary.wiley.com/terms-and-conditions) on Wiley Online Library for rules of use; OA articles are governed by the applicable Creative Commons License

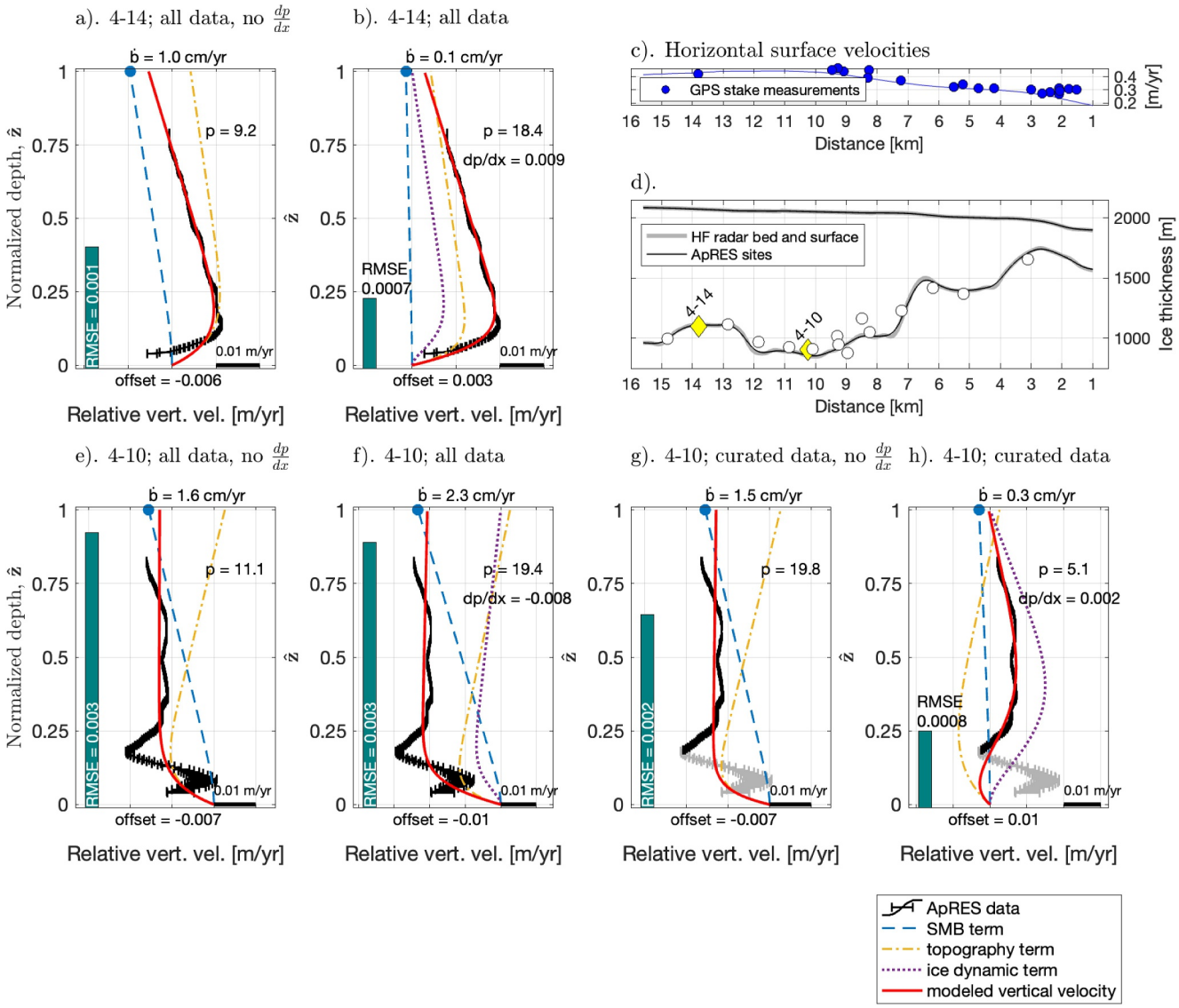

Figure 8. Kinematic model fits to individual ApRES profiles. (a and b). Model fits (red lines) to site 4-14 data (black error bars) both (a) with no ice dynamic term and (b) including the ice dynamic term. The blue dashed line is the SMB-accommodating term; the yellow dashed line is the topography-driven term; the purple dotted line is the ice dynamic term. Green bars represent the model-data root mean square error, with units of m/yr. (c) Horizontal surface velocities used to calculate the model velocity components. (d) Ice surface and bedrock elevations (on the same horizontal scale as in c) from the profiling radar, used to calculate H, $\frac{dH}{dx}$, S, and $\frac{dS}{dx}$. ApRES sites are plotted along flow (white dots and yellow diamonds), with the vertical coordinate representing ice thicknesses from the ApRES data. (e–h). Model fits to site 4–10 data with (e) the full data profile and no ice dynamic term, (f) all data and including all velocity terms, (g) a curated data set and no ice dynamic term, and (h) the curated data set and including all velocity terms.

3.3. Individual Site Model-Data Fits

In past applications of the kinematic model to interpret ApRES data near a divide, the SMB-accommodating term was sufficient to explain most of the vertical velocity structure (Fudge et al., 2023). At the Allan Hills, however, steep topography and slow SMB rates mean that the topography-driven term (term 2 of Equation 2) cannot be neglected.

In the kinematic model, the topography-driven vertical velocity component is constrained in sign and approximate magnitude by measurements of surface/bedrock elevations and of surface horizontal velocities. The modeled term corroborates some observed strain-rate reversals with depth. For example, Figure 8a plots the model fit to the 4-14 data using the SMB-accommodating and topography-driven vertical velocity components.

21699011, 2026, 11, Downloaded from https://agupubs.onlinelibrary.wiley.com/doi/10.1029/2026JF009592 by British Antarctic Survey, Wiley Online Library on [27/11/2026]. See the Terms and Conditions (https://onlinelibrary.wiley.com/terms-and-conditions) on Wiley Online Library for rules of use; OA articles are governed by the applicable Creative Commons License

21699011, 2026, 11, Downloaded from https://agupubs.onlinelibrary.wiley.com/doi/10.1029/2026JF009592 by British Antarctic Survey, Wiley Online Library on [27/11/2026]. See the Terms and Conditions (https://onlinelibrary.wiley.com/terms-and-conditions) on Wiley Online Library for rules of use; OA articles are governed by the applicable Creative Commons License

At about 15% of the ice thickness off the bed, the measured vertical velocity profile changes from increasing velocities with distance off the bed (vertical extension) to decreasing velocities (compression). This strain-rate reversal is consistent with the model prediction of upward velocities at depth due to horizontal flow up the bedrock slope. Inclusion of the topography-driven term similarly allows the model to match the structure and magnitudes of observed velocities at sites 5-6, Xc, and 5-5 (Figures S8 and S12 in Supporting Information S1). However, at sites 4-15, 5-5, 4-8, and 4-6, the modeled topography-driven term cannot be reconciled with the observed velocities. Additional description of these model fits is provided in Text S4 in Supporting Information S1.

The kinematic model can recreate at most two local maxima or minima: one from the flow over topography and another from the ice dynamic term (Figure 7). Some ApRES-observed vertical velocities are therefore incompatible with the kinematic model. For example, the basal signal at site 4-10 (Figure 8d) has an "S" shape with increasing vertical velocities off the bed (extension) that transition to decreasing velocities (compression) and back to extension, all within the deepest 25% of the ice column. The data at site Xd show a similar signal, while site 4-9 has a reversed "S" shape. These vertical velocities fall outside the possible solution space for the model.

Model-data disagreements may indicate measurement artifacts in the deepest ice. The ApRES SNR is lowest close to the bed (Figures 2a, 2e, and 2h), while the potential for Lagrangian errors or off-nadir reflections is highest (Section 2.5). Of course, some of the excluded data may describe real velocities that are incompatible with the model's Lliboutry shape functions, which require the horizontal velocity profile to change smoothly with depth. The "S" shaped basal data are discussed at greater length in Section 5.3.

3.4. Data Curation

Using the model-data fits from Section 3.3 and Text S4 in Supporting Information S1, we construct a curated set of data, which isolates the most robust set of data for each ApRES site (Figure S7 in Supporting Information S1). We exclude englacial oscillations that may result from rotational offsets in the antenna setup between acquisitions (Section 2.4). We also choose to exclude basal velocities that cannot be corroborated by the model at the individual ApRES sites. The curated profiles are used in the following Section 4.1 where we conduct a model optimization to observed velocities at all sites along the track 4 flowband. Restricting analysis to the curated data set allows for a flowband representation of the well-behaved aspects of the data and enables more meaningful investigation into the changes in deformation across the different ApRES sites.

The data excluded in the curation process include:

- large velocity oscillations at sites 4-13 and 4-12, which may be attributable to rotational offsets in the antenna setup
- the "S" shaped basal velocities at sites 4-10, Xd, and 4-9, which show multiple sharp inversions that are impossible to match with the kinematic model (Section 3.3)
- basal vertical velocity observations that are inconsistent with the modeled topography-driven component of vertical flow (4-15, 5-5, 4-8, 4-6)
- The 4-7 profile, where the model fit to the data requires ablation of ∼10 cm/yr (2× the highest rate observed by Spaulding et al., 2012) to balance strong topography-driven vertical flow up the steep bedrock slope

4. Flowband Modeled and Measured Velocities

The individual-site optimizations in Section 3 corroborate the data and demonstrate the importance of topography-driven vertical velocity components at the Allan Hills. However, fitting for ice flow parameters at each site in isolation neglects the interdependence of the modeled deformation profiles. Sites 4-10 and Xd are located within 200 m of each other; other sites are spaced about one ice thickness (∼1,000 m) along radar track 4. To change from $p = 1$ to $p = 20$ over 1 km requires a gradient of $\frac{dp}{dx} = 0.02$, producing a modeled ice dynamic velocity component that dominates the vertical flow. The value of $p(x)$ along track 4 should therefore account for the entire ApRES vertical velocity survey at once.

In this section, we consider model-data comparisons across the track 4 flowband (the volume bounded by two nearby flowlines, Parrenin & Hindmarsh, 2007; Waddington et al., 2007). We restrict analysis to the curated data set. By design, the curated velocities are compatible with the kinematic model terms; however, it is not obvious

21699011, 2026, 11, Downloaded from https://agupubs.onlinelibrary.wiley.com/doi/10.1029/2026JF009592 by British Antarctic Survey, Wiley Online Library on [27/11/2026]. See the Terms and Conditions (https://onlinelibrary.wiley.com/terms-and-conditions) on Wiley Online Library for rules of use; OA articles are governed by the applicable Creative Commons License

that the model can represent the entire data set at once, with the additional constraints on the ice dynamic term that this implies. In Section 4.1, we construct an optimization problem for flowband fits to the curated data set to test whether the ApRES survey captures reasonable changes in deformation across track 4. We discuss the velocities and SMB rates from those flowband model optimizations in Section 4.2. Finally, in Section 4.3 we use the ice mass continuity over the flowband as a reality check on the model assumptions, demonstrating that 3-D topography effects may be important in zones with steep bedrock slopes.

4.1. Optimizing the Flowband Model Against All Curated Vertical Velocities

We calculate vertical velocities across track 4 using (a) the same surface/bedrock elevation and horizontal velocity constraints as in the individual-site profiles from Section 3.2 (Conway & Campbell, 2017; Shaya, Manos, Banerjee, et al., 2026; Spaulding et al., 2012) and (b) parameter fields $\dot{b}(x)$ and $p(x)$, which now vary smoothly along the flow direction, x.

In the inverse problem, we choose to solve for $\dot{b}$ and $q = \log(p)$ at each ApRES site and at the ends of the track 4 domain. We interpolate $\dot{b}(x)$ and $p(x)$ using a Piecewise Cubic Hermite Interpolating Polynomial fit to the data (the `pchip` function in MATLAB), which preserves monotonicity and avoids sharp corners in the data. We additionally solve for a depth-constant data offset a_i at each ApRES site. The parameter ranges are the same as those used in Section 3.2, with the exception of the bounds on p. In the individual-site optimizations, p was allowed to vary between 0.1 and 20; however, model fits to the curated data all found p values greater than one (Figure S9 in Supporting Information S1). In the flowband optimization, we therefore confine p to the range from 1 to 20, which is consistent with expectations for ice flow away from a divide (Raymond, 1983).

The gradient $\frac{dp}{dx}$ is not explicitly solved for in the flowband optimization; instead, this term is calculated from the interpolated $p(x)$. With no a priori expectation for the values of $p(x)$ or $\frac{dp}{dx}$, the parameter space is large. We thus introduce a smoothing term in the optimization that penalizes large changes in $\frac{dq}{dx}$ (for $q = \log p$). While this smoothing does not solve the problem of non-uniqueness in the solution space, it restricts analysis to regions of the parameter space where the change in $q(x)$ along track 4 drives a reasonable ice dynamic contribution to the model velocities. The results of the optimization, especially with low regularization, are additionally sensitive to the initial guess in the optimization. We initialize the parameter search with $p(x) = 8$, $a_i = 0$, $\dot{b}(x) = 0$. Further details of the non-uniqueness are discussed in Text S5 in Supporting Information S1.

We apply the MATLAB nonlinear least squares optimization function `lsqnonlin` (The MathWorks, Inc, 2024) with the trust-region-reflection algorithm (Coleman & Li, 1996) to minimize the objective function:

$$\sum_{j=1}^{16}\sum_{\hat{z}}\left(w(x_j,\hat{z}_i)-\mathcal{W}(x_j,\hat{z}_i)-a_j\right)^2+\lambda\sum_{x}\left(\frac{d^2q(x)}{dx^2}\right)^2 \tag{4}$$

for model velocities $w(x_j, \hat{z}_i)$ and curated data profiles $\mathcal{W}(x_j, \hat{z}_i)$ at the 16 ApRES sites. The second summation term represents the smoothing constraint with weighting λ.

4.2. Flowband Model-Data Optimizations

The velocity solutions depend on the choice of λ, which determines the penalty for high curvature in $p(x)$. We calculate solutions for λ varying from 0.001 to 100. The data and regularization costs for each λ are plotted in Figure S16 in Supporting Information S1; the shape function p parameters are shown in Figure S17 in Supporting Information S1. With minimal regularization ($\lambda = 0.001$), the solution for $p(x)$ has several peaks and troughs. As λ increases to 0.2, the trough in $p(x)$ at site 4-5 vanishes. Overall, the p parameter is high at 4-14, lower near 4-10 through 4-8, and then high again in the shallow sites 4-6 and 4-5. Continuing increases to λ further mute the curvature of $p(x)$. A weighting of $\lambda = 0.2$ balances the data and regularization cost (Figure S14 in Supporting Information S1); we therefore use that value in further analyses (Engl & Grever, 1994).

Figure 9 shows the velocities from the flowband optimization to the curated data (omitting site 4-7) with $\lambda = 0.2$. Panel 9b compares the ApRES data with profiles of model vertical velocities at each site. While there are small deviations from the observations, especially in the deepest ice, the model matches the magnitude and shape of the

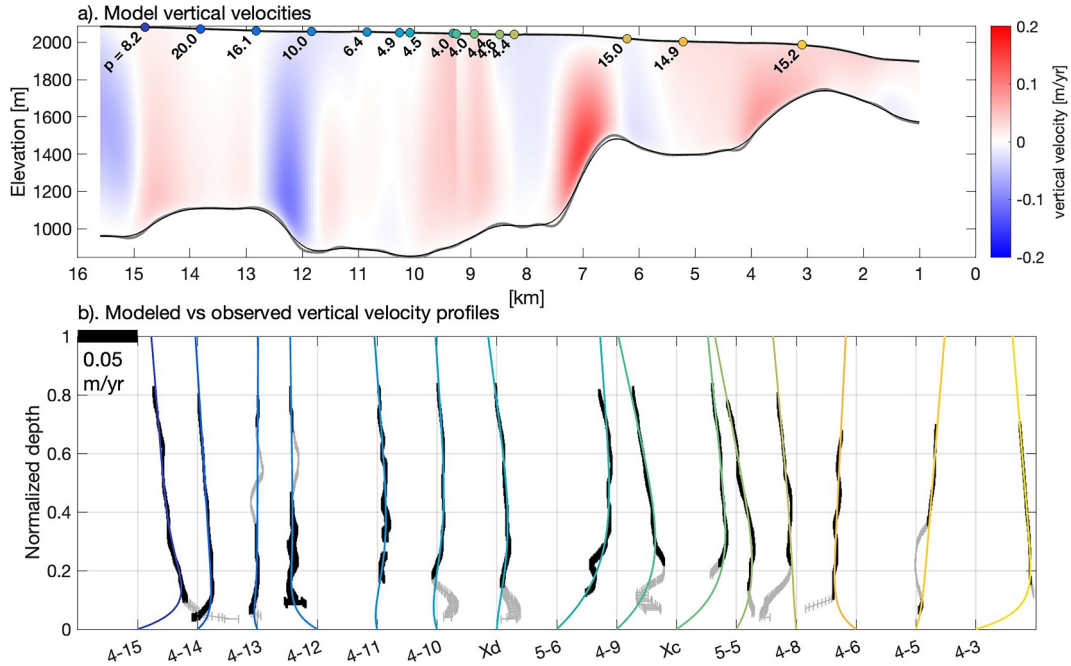

Figure 9. Flowband model-data comparison with the curated ApRES data set (also excluding site 4-7) and $\lambda = 0.2$. Note that the optimization is non-unique and this figure represents only one possible solution. (a) Model vertical velocities along track 4. (b) Curated ApRES relative vertical velocity data (black error bars, excluded data in gray) compared to model velocity profiles at the ApRES sites (colored lines). All model velocities are zero at the bed. The horizontal grid spacing corresponds to an 0.05 m/yr relative vertical velocity.

curated vertical velocity data. All model velocity solutions are strongly influenced by ice thickness gradients. The model shows upward flow when the ice thickness is decreasing (as ice flows up the bedrock bump and the steep slopes at kilometer 7) and downward flow when ice thickness is increasing (flowing down the bedrock bump). Contributions from the ice dynamic term help explain the multiple strain-rate reversals at sites 4-10 and Xd (near kilometer 10). The SMB rates predicted in the flowband model optimizations are similar for various choices of λ; they are also similar to the SMB rates predicted in the individual-site model-data fits (Figure 10a).

4.3. Mass Continuity Over the Flowband

Unlike other applications of the kinematic model (Fudge et al., 2023), we do not calculate mean horizontal velocities from the balance of mass flux. Instead, following (Grinsted et al., 2003), we input the observed surface horizontal velocities and assume that convergence or divergence in the cross-flow dimension maintains mass continuity. Here, we explore that assumption by approximating the lateral flow divergence and calculating the SMB rate that would be required to preserve ice mass continuity.

Neglecting basal melting and changes to the surface elevation, the SMB rate required to preserve ice mass continuity is (Pettit et al., 2014):

$$\dot{b}(x)_{\text{mass cont.}} = \frac{1}{W}\frac{\partial(\bar{u}HW)}{\partial x} \tag{5}$$

where $W(x)$ is the flowband width. We constrain $W(x)$ at the Allan Hills using the surface velocity measurements. Radar track 4 is an approximate flowline (see Figure 1), but there is a non-zero component of transverse flow, meaning that true streamlines will cross the track. Instead, we use the observed transverse strain rate to calculate $W(x)$ (see Text S6 in Supporting Information S1 for details).

Figure 10b shows $\dot{b}_{\text{mass cont.}}$ along track 4 for the flowband velocity solution plotted in Figure 9. Equation 5 predicts several peaks in the $\dot{b}_{\text{mass cont.}}$, including an accumulation rate of 12 cm/yr at kilometer 12.5 as the ice

21699011, 2026, 11, Downloaded from https://agupubs.onlinelibrary.wiley.com/doi/10.1029/2026JF009592 by British Antarctic Survey, Wiley Online Library on [27/11/2026]. See the Terms and Conditions (https://onlinelibrary.wiley.com/terms-and-conditions) on Wiley Online Library for rules of use; OA articles are governed by the applicable Creative Commons License

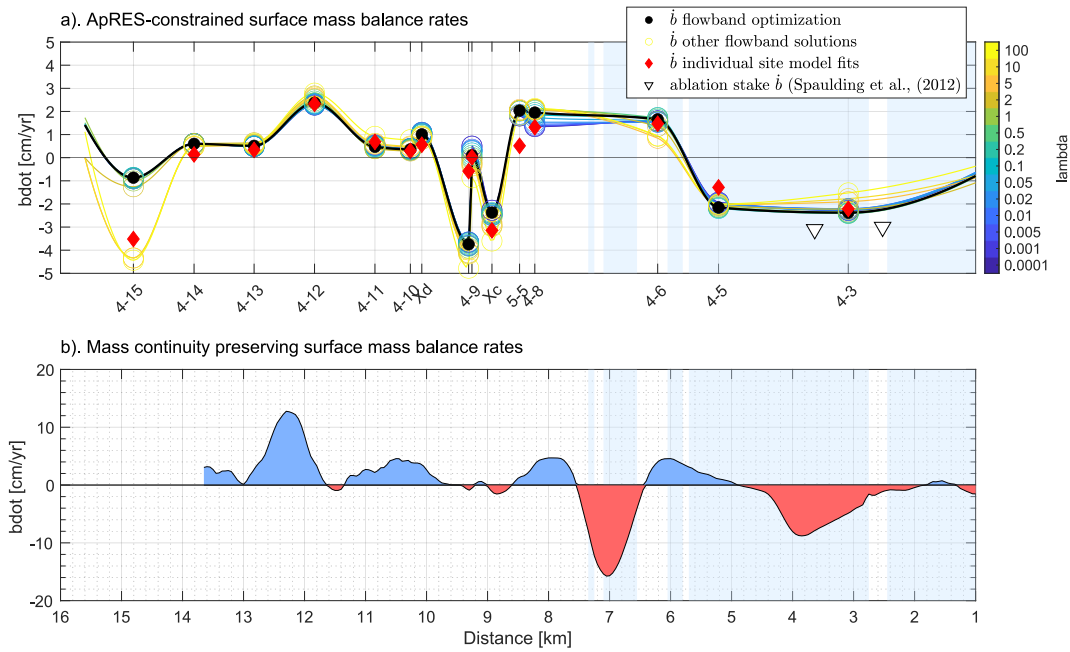

Figure 10. Mass balance from model optimizations and ice mass continuity. (a) Surface mass balance (SMB) rates from flowband model optimizations (colored dots and lines). The solution corresponding to Figure 9 ($\lambda = 0.2$) is plotted in black. The red diamonds show SMB rates from individual-site model optimizations. Also plotted are the ablation stake constraints in the accumulation zone. The background shade of blue/white indicates ice/snow cover visually identified from satellite imagery. (b) Steady state mass continuity-preserving SMB rates calculated from $\bar{u}$ (from u_{surf} and the model p values), $H(x)$, and $W(x)$. Note the increase in scale on the y-axis relative to (a).

flows down the bedrock bump and an ablation rate of −19 cm/yr at kilometer 7 as the ice thins and flows up a steep bedrock slope.

Spatial variability of SMB is poorly constrained by data at the Allan Hills, and peaks in accumulation and ablation rates along the flowband are possible. The peaks in $\dot{b}_{\text{mass cont.}}$, however, are an order of magnitude larger than the observed accumulation and ablation rates of +3 to −5 cm/yr (Dadic et al., 2015; Spaulding et al., 2012). The mass balance anomalies at sites with steep bedrock slopes reveal the limitations of the flowband assumptions at the Allan Hills. The flowband model and the equation for ice mass flux assume that $\bar{u}$ and H are constant in the cross-flow direction. In reality, cross-flow gradients in the basal topography exist (Figure S19 in Supporting Information S1) and are expected to affect the ice mass flux, both by changing the effective bedrock thickness for a slice of the flowband and by enabling 3-D variations in the ice flow direction.

5. Discussion

The individual-site fits (Section 3) and flowband fits (Section 4) provide insight into the vertical velocity components captured in the ApRES data. In Section 5.1, we discuss the contributions from the topography-driven, ice dynamic, and SMB-accommodating terms. In Section 5.2, we discuss the kinematic model framework for interpreting ApRES data in regions of low SMB and steep topography, and we provide recommendations for future surveys of BIAs. Finally, in Section 5.3 we describe the basal ice signal and we explore implications to the age scale of a proposed intermediate depth ice core at the Allan Hills.

5.1. Characterizing Ice Flow at the Allan Hills

Here, we discuss insights into the ice flow from both the individual-site and flowband model-data comparisons. We structure this discussion using the kinematic model vertical velocity terms ordered from greatest to least data constraints: starting with the topography-driven vertical velocity component, moving to the ice dynamic velocities, and ending with the SMB-accommodating term.

21699011, 2026, 11, Downloaded from https://agupubs.onlinelibrary.wiley.com/doi/10.1029/2026JF009592 by British Antarctic Survey, Wiley Online Library on [27/11/2026]. See the Terms and Conditions (https://onlinelibrary.wiley.com/terms-and-conditions) on Wiley Online Library for rules of use; OA articles are governed by the applicable Creative Commons License

21699011, 2026, 11, Downloaded from https://agupubs.onlinelibrary.wiley.com/doi/10.1029/2026JF009592 by British Antarctic Survey, Wiley Online Library on [27/11/2026]. See the Terms and Conditions (https://onlinelibrary.wiley.com/terms-and-conditions) on Wiley Online Library for rules of use; OA articles are governed by the applicable Creative Commons License

The topography-driven vertical velocities are a significant component of the ice flow field and the ApRES measurements. In the kinematic model, the sign and approximate magnitude of the topography-driven velocities (term 2 in Equation 2) are determined by the observed bed and surface elevation profiles and the surface horizontal velocities. Using these data constraints, the topography-driven velocities are predicted to have magnitudes greater than or equal to the SMB-accommodating term (Figure S8 in Supporting Information S1). Incorporating the topography-driven term in model fits to the data allows the model to reproduce observed strain-rate reversals (e.g., at site 4-14, Figure 8a). The individual-site fits provide a strong corroboration of ApRES data at sites 4-14, 5-6, Xc, and 5-5 where the modeled topography-driven term is consistent with the observations.

At several other sites, the modeled topography-driven term is inconsistent with the ApRES relative vertical velocities, indicating either basal measurement effects or ice flow complexity that exceeds the model capabilities. In particular, the ApRES data at site 4-7 cannot be fit by the model using the observed steep bedrock slope. At 4-7, the mass continuity-preserving SMB (Equation 5) additionally predicts an implausibly high ablation rate of −19 cm/yr. We interpret these data-model mismatches as evidence of cross-track variations in the ice flow. Additional profiling radar tracks near site 4-7 reveal that the ice thickness change is not uniform in the cross-flow direction (Figure S17 in Supporting Information S1). Ice may flow around bedrock obstacles, maintaining ice mass continuity and damping the effect of steep topographic gradients. Future work could compare ApRES velocities on steep bedrock slopes with kinematic models constructed using an "effective ice thickness gradient" that accounts for the variation in H and dH/dx over the cross-track dimension. This extension of the model would require high resolution mapping of the bedrock in the along flow and transverse directions.

The ice dynamic component of vertical velocity, which describes vertical velocities that result from changes to the horizontal velocity shape function along flow, is bounded but otherwise unconstrained in the individual-site fits. In contrast, the ice dynamic term in the flowband optimization is sensitive to the surrounding ApRES sites. Despite the additional constraints, the flowband model can fit the curated ApRES data set nearly as well as the individual-site fits. The RMSE for the flowband result (Figure 9) is 0.0013 m/yr; in comparison, the RMSE for all individual-site fits to the curated data is 0.0011 m/yr. Overall good model fits to the data are partly a consequence of the data curation, which selects for data that are compatible with the model velocity terms and the topographic constraints. However, the order-of-magnitude similarity between the residuals from individual-site and flowband model optimizations indicates that the ApRES survey captures reasonable variations in deformation along track 4.

The model-data comparisons also suggest that ApRES may be useful for constraining SMB in BIAs. In both the individual-site and flowband model optimizations, the SMB-accommodating velocities have the most freedom of all three velocity components due to the lack of robust data constraints. However, Figure 10a shows a broad agreement in inferred SMB rates between the individual-site fits (red diamonds) and flowband optimizations (colored circles) to the curated data.

In theory, calculating SMB rates from ApRES data referenced to the bed should be straightforward because the velocity trend near the surface, neglecting firn compaction, is dominated by the SMB-accommodating term (Figure 7). However, our combined relative vertical velocity profiles are not referenced to an absolute datum, due to uncertainties from the low SNR in the near-bed signal (including the possibility of phase-wrapping that cannot be resolved) and potential errors from off-nadir contributions and Lagrangian effects. The model-data optimizations include a depth-constant offset that can shift the data by ±0.2 m/yr; changes to this offset can enable large changes in $\dot{b}$, as occurs in Figures 8a and 8b with the introduction of the ice dynamic term.

The consistency between the inferred SMB rates for different model optimizations (Figure 10) suggests that ApRES data combined with the kinematic model may offer a different approach for constraining the SMB. Validating the ApRES-inferred SMB, however, requires further measurements of accumulation and ablation in the snow-covered areas. While stake surveys have measured ablation on the exposed blue ice (Spaulding et al., 2012), these measurements are complicated over snow cover because of the rough surface, migrating sastrugi, and the potential for enhanced wind scour or deposition around the stake. The SMB is expected to change sign from accumulation upstream (Dadic et al., 2015) to ablation that removes the snow and exposes blue ice (Dadic et al., 2013), however the location of this transition—or of multiple transitions—remains largely unknown.

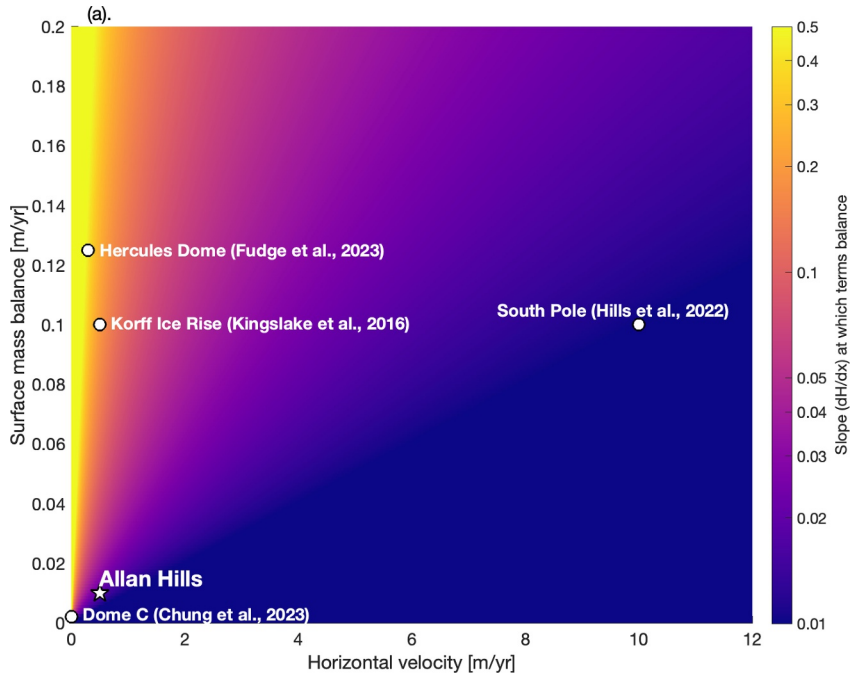

Figure 11. (a) Ice thickness gradient $\left(\frac{dH}{dx}\right)$ for which the surface mass balance-accommodating flow and the topography-driven flow balance each other out ($\eta = 1$). Dots mark the accumulation rate and horizontal velocities of some Antarctic sites that have been studied with Autonomous phase-sensitive Radio Echo Sounder surveys.

5.2. A Framework for Interpreting ApRES From BIAs

As the search for ancient ice in Antarctic BIAs continues, ApRES interferometry will be a key method for evaluating ice flow and predicting age structures. Interpreting ApRES data in BIAs, however, is complicated by the very slow deformation and the steep bedrock slopes at these regions. The Allan Hills data set, comprising 3 years of measurements co-located with GNSS velocities and ground penetrating radar lines, provides a new perspective on survey design and data analysis to meet these challenges. Here, we introduce a criteria to identify ice sheet areas where the model framework is highly relevant to interpreting ApRES data, and we provide recommendations for surveys in those regions.

The topography-driven component of vertical velocities is significant when term 2 of Equation 2 is large relative to the SMB-accommodating deformation (term 1). We introduce the non-dimensional number $\eta = \frac{\dot{b}}{UdH/dx}$, which represents the balance between these two terms. When $\eta \gg 1$, the SMB-accommodating flow will dominate the vertical velocities; when $\eta \ll 1$, the topography-driven flow will dominate. At most ice sheet sites, the characteristic values of $\dot{b}$ and U change slowly in space; however, η may vary over relatively short spatial scales due to variable ice thickness gradients in regions of rough bedrock topography. In Figure 11, we therefore plot the ice thickness gradient $\frac{dH}{dx}$ needed for the SMB-accommodating and topography-driven velocity terms to balance each other ($\eta = 1$) for various characteristic values of U and $\dot{b}$. At Hercules Dome and Korff Ice Rise, a relatively high ice thickness gradient (~0.2–0.5) is needed for the topographic flow to become relevant. At the South Pole, however, the faster horizontal velocities mean that the flow over topography may be an important term, even for a small ice thickness gradient (~0.01). The kinematic model is a useful tool for describing ice flow and predicting age structure at many locations (see Fudge et al., 2023), but it is especially valuable for interpreting ApRES data when η is small.

The slow deformation of BIAs means that minor inconsistencies in the ApRES interferometric measurement can create significant apparent velocities. This paper makes use of redundancy across the 3 years of measurements and multiple polarizations at each site to isolate the real signal from errors caused by offsets in the antenna spacing (Section 2.3) and rotation (Section 2.4). Future deployments in BIAs and other slow-flowing regions should control the antenna positions to the centimeter-scale and within $\pm 1°$ rotation, either using flags at all four corners

21699011, 2026, 11, Downloaded from https://agupubs.onlinelibrary.wiley.com/doi/10.1029/2026JF009592 by British Antarctic Survey, Wiley Online Library on [27/11/2026]. See the Terms and Conditions (https://onlinelibrary.wiley.com/terms-and-conditions) on Wiley Online Library for rules of use; OA articles are governed by the applicable Creative Commons License

21699011, 2026, 11, Downloaded from https://agupubs.onlinelibrary.wiley.com/doi/10.1029/2026JF009592 by British Antarctic Survey, Wiley Online Library on [27/11/2026]. See the Terms and Conditions (https://onlinelibrary.wiley.com/terms-and-conditions) on Wiley Online Library for rules of use; OA articles are governed by the applicable Creative Commons License

or, if practical for a given site, deploying ApRES antennas that remain in place for the duration of the measurement. Orienting the antennas along the ice fabric horizontal axes (if known) will also reduce the apparent velocity errors caused by small rotation offsets.

We recommend aligning ApRES measurements along a flowline, co-located with measurements of surface horizontal velocities and bedrock topography. Together with profiling radar measurements of the ice bed and surface elevation, these data constrain the topography-driven vertical velocity component. Additional profiling radar tracks are helpful to assess the 3-D geometry and to establish whether assumptions of no cross-flow variation in H are appropriate. To evaluate changes in ice flow across a BIA, we recommend spacing ApRES sites at approximately one ice thickness or less. In the model, changes in the ice flow parameter $p(x)$ along flow drive the ice dynamic contribution to vertical velocities. At approximately 1 km distance from each other, our ApRES deformation profiles are not independent, providing constraints on $p(x)$ in the flowband inversions. Finally, although not included in our analysis due to challenges in observing cm-scale accumulation, SMB rates or surface vertical velocity measurements would allow the ApRES data to be referenced to an absolute datum, eliminating the need for the offset parameter a and reducing the free parameters in the model optimization.

5.3. Basal Ice Units and an Intermediate Depth Ice Core Site

The profiling radar and ApRES data reveal a change in the scattering properties of the deep ice downstream of the bedrock bump, with parallels to basal ice units that have been identified widely across Antarctica with airborne and ground-based radar (e.g., S. Yan et al., 2026). Basal ice units are characterized by the lack of coherent layering in the radargrams, which can be due to either a lack of observable scattering (e.g., Drews et al., 2009; MacGregor et al., 2015) or incoherent scattering (e.g., Franke et al., 2023; Mutter & Holschuh, 2025; D. A. Young et al., 2025). How this ice deforms is critical to understanding both the flow of ice sheets and the preservation of old ice (Chung et al., 2025; Lilien et al., 2021). We focus this section of the discussion around a proposed intermediate depth ice core site near sites 4-10 and Xd. The ice column near these sites is predicted to contain a 1 Ma continuous climate record (Kehrl et al., 2018), which would (a) give valuable insight into past climate variability over glacial-interglacial timescales and (b) provide context for the ancient but discontinuous shallow ice cores drilled farther down flow (e.g., Shackleton et al., 2025).

Sites 4-10, Xd, and 4-9 lie in a basin in the bed topography downstream of a 200 m relief bedrock bump. As ice flows over this obstacle, the deepest dated englacial layer (~250 ka) doubles in fractional ice thickness off the bed (Figure 1). In the deepest 200 m (below the 250 ka layer), the 7 MHz ground penetrating radar (Conway & Campbell, 2017) reveals no continuous englacial reflectors. Meanwhile, at sites 4-10, Xd, and 4-9, the backscattered ApRES power peaks ~250 m off the bed, then decreases steeply down to the bed (Figure 2e). This pattern of attenuation contrasts with the more linear power profiles of ApRES measurements elsewhere along track 4 (Figure 2a).

At these sites, the basal ApRES relative vertical velocity profiles have an "S" shape, characterized by two sharp strain-rate reversals in the deepest quarter of the ice column. The signal likely represents some combination of measurement errors and real deformation. The error bars on the basal velocities are large due to the lower SNR of the near-bed data points, and the phase coherence magnitude between measurements used in the interferometric processing drops steeply in the deepest ~250 m (Figure S5b in Supporting Information S1). The "S" shape is incompatible with the kinematic model. However, the signal remains consistent across different years and polarizations of data as well as nearby sites. This is a promising data set for exploring interferometric measurements of deformation in basal units, because the moderate ice thickness (~1000 m) means the signal-to-noise ratios enable resolution of velocities all the way to the bed.

The anomalous basal scattering at the Allan Hills may result from several mechanisms associated with Antarctic basal units. Disruptions to the englacial layering (Drews et al., 2009) could occur due to the steep bedrock relief and the complicated ice flow history of the region. In the shallower downstream area of the Allan Hills, ice cores drilled to bedrock have a discontinuous and inverted age scale (Higgins et al., 2015; Y. Yan et al., 2019). Englacial layering at core ALHIC2201 is mostly bed-parallel, suggesting that folding occurred upstream or in a past flow regime (Kirkpatrick et al., 2025). If a non-stratigraphic basal unit exists in the ~1000 m ice, it could be an upstream source for the disturbed packets of ancient ice. At other ice sheet locations, debris entrainment from basal freeze-on is associated with incoherent scattering and basal units (Franke et al., 2023; Winter et al., 2019), although the frozen bed of the Allan Hills (Kehrl et al., 2018) precludes freeze-on in the present day. Finally,

changes to the ice fabric may play a role in the basal scattering as observed at other ice core locations (Mutter & Holschuh, 2025).

Disturbed layers or incoherent scattering will complicate the interferometric deformation profiles. The ApRES data likely measure some basal ice velocity components, and we do not exclude the possibility that some or all of the "S" shaped deformation profile is real. However, interpretations of ApRES interferometry typically assume that layers are flat and specular (T. J. Young et al., 2018). If the backscattered power instead arrives from off-nadir, the interferometric processing will record deformation along an off-vertical axis. Depending on the layer geometry and the presence of point scatterers within the radar footprint, the ApRES data may superimpose deformation signals from several off-vertical axes. The deformation profiles are further complicated by Lagrangian errors near the bed. In the case of coherent englacial layers, the movement of the ApRES antennas relative to the basal ice parcels introduces an apparent layer-following velocity (Hills et al., 2022). If scatterers are incoherent, measurements from different years may instead capture different reflectors, explaining the low phase coherence magnitude in the basal ice and introducing measurement artifacts near the bed.

Our results suggest that the smooth vertical deformation profile employed by Kehrl et al. (2018) may be too simplistic for the basal ice in this region. While the data do not specifically exclude the possibility of a continuously deforming ice column, the complicated scattering properties and "S" shaped interferometric profile of the deepest ice—together with the increase in fractional thickness off the bed of the deepest dated layer—suggest that this ice may have distinct chemical or rheological properties. The basal ice may be more resistant to flow (e.g., Chung et al., 2023) or potentially even overturning (Meyer & Creyts, 2017). The impact on the depth-age relationship is unclear. If the basal ice is relatively non-deforming, like it appears to be at Little Dome C (Chung et al., 2025), a continuous depth-age relationship may exist only in the upper ∼1,000 m of the ice column above the basal ice unit, further thinning the ∼1 Ma ice. This scenario would leave ∼200 m of non-stratigraphic ice near the bed, perhaps including ancient ice (given the recovery of 6 Ma ice packets from shallower regions of the Allan Hills, Shackleton et al., 2025).

Further improvement to our understanding of ice deformation in the study region will require dedicated modeling and continued geophysical investigation. On the modeling front, integration of internal layers (e.g., Kehrl et al., 2018) with our vertical velocities can be used to test hypotheses about deformation. Further geophysical constraints may include fabric analysis from polarimetric ApRES as well as future radar campaigns that can provide profiling estimates of the ice fabric (e.g., Holschuh et al., 2026). Additionally, collection of more horizontal and vertical velocities will allow better constraints on the SMB rates and ice-flux divergence, which both remain underconstrained by existing data.

6. Conclusions

We present the first ApRES survey of englacial vertical velocities in a blue ice area: the Allan Hills, Antarctica. Our analysis provides a blueprint for recovering high-quality englacial vertical velocity measurements in BIAs with very slow ice flow. To resolve near-zero velocities, we identify and account for measurement errors that could reasonably be neglected in faster flowing sites. These include (a) small (∼10 cm) changes to the antenna spacing, which cause apparent compression/extension signals in the top 200 m and (b) small (<5°) offsets to the antenna rotation relative to the ice fabric axes, which introduce oscillatory apparent velocities superimposed on the mean deformation.

We interpret the observed vertical velocities using a kinematic model that partitions flow into SMB-accommodating, topography-driven, and ice dynamic components. Constrained by observed surface horizontal velocities and bedrock topography, this simple two-dimensional model explains most of the measured velocity profiles, both at individual sites and along the 15 km flowband. The comparisons demonstrate that flow over bedrock topography can contribute substantially to vertical velocities in blue ice areas and must be considered when interpreting ApRES measurements. Where bedrock slopes are particularly steep, however, the modeled velocities and mass fluxes are inconsistent with observations, likely reflecting three-dimensional flow around bedrock obstacles.

New observations and models of the ice flow that preserve old ice records will be needed to recover older and more pristine records. One potential region is downstream of the bedrock bump at 10 km along our flowband. The radar data exhibit both anomalous velocity and scattering signals, and we propose that there may be a ∼200 m

21699011, 2026, 11, Downloaded from https://agupubs.onlinelibrary.wiley.com/doi/10.1029/2026JF009592 by British Antarctic Survey, Wiley Online Library on [27/11/2026]. See the Terms and Conditions (https://onlinelibrary.wiley.com/terms-and-conditions) on Wiley Online Library for rules of use; OA articles are governed by the applicable Creative Commons License

21699011, 2026, 11, Downloaded from https://agupubs.onlinelibrary.wiley.com/doi/10.1029/2026JF009592 by British Antarctic Survey, Wiley Online Library on [27/11/2026]. See the Terms and Conditions (https://onlinelibrary.wiley.com/terms-and-conditions) on Wiley Online Library for rules of use; OA articles are governed by the applicable Creative Commons License

thick basal unit of unknown stratigraphic properties in this zone, where a ∼1,000 m depth ice core has been proposed. This project has characterized englacial deformation at the BIA with the oldest known ice on Earth and provides a first step toward improved depth-age modeling of the upstream Allan Hills area.

Conflict of Interest

The authors declare no conflicts of interest relevant to this study.

Availability Statement

The GNSS surface velocities (Shaya, Manos, Banerjee, et al., 2026) are archived at https://doi.org/10.15784/602026. The 7 MHz ground-penetrating radar profiles (also discussed by Kehrl et al., 2018) are archived at https://www.usap-dc.org/view/dataset/601005. The repeat ApRES data (Shaya, Manos, Li, et al., 2026) are archived at https://doi.org/10.15784/602075.

Acknowledgments

This work was supported by the U.S. National Science Foundation Center for Oldest Ice Exploration (NSF COLDEX), an NSF Science and Technology Center (NSF 2019719). We thank the NSF Office of Polar Programs, the NSF Office of Integrative Activities, and Oregon State University for financial and infrastructure support, and the NSF Antarctic Infrastructure and Logistics Program and the Antarctic Support Contractor for logistical support. COLDEX integrates activities in ice coring and analysis, Antarctic exploration and ice sheet modeling, education, knowledge transfer, and broadening participation. All Center components and participants are essential to its success and contribute to the shared infrastructure that underpins all COLDEX products, including this publication. We thank the I-188-M (2022–23) and I-187-M (2023–24, 2024–25) Antarctic field teams, including camp and field safety personnel Tim Farr, Ema Mayo, Ash Goverman, and Kelcie Meyer; Ice Drilling Program (IDP) drillers Elizabeth Morton, Mike Jayred, Tanner Kuhl, and Andrew Haala; and field team scientists Asmita Banerjee, Edward Brook, Austin Carter, Jenna Epifanio, John Higgins, Abigail Hudak, Julia Marks Peterson, Sarah Shackleton, Jacob Chalif, Fairuz Ishraque, Liam Kirkpatrick, and Jeffrey Severinghaus. We thank Kenn Borek Air for logistical support. We would also like to thank the editor and two reviewers for their helpful comments.

References

Arthern, R. J., J. Corr, H. F., Gillet-Chaulet, F., Hawley, R. L., & Morris, E. M. (2013). Inversion for the density-depth profile of polar firn using a stepped-frequency radar. *Journal of Geophysical Research: Earth Surface*, *118*(3), 1257–1263. https://doi.org/10.1002/jgrf.20089

Atkins, C., Barrett, P., & Hicock, S. (2002). Cold glaciers erode and deposit: Evidence from Allan Hills, Antarctica. *Geology*, *30*(7), 659–662. https://doi.org/10.1130/0091-7613(2002)030<0659:CGEADE>2.0.CO;2

Brennan, P., Lok, L., Nicholls, K., & Corr, H. (2014). Phase-sensitive FMCW radar system for high-precision Antarctic ice shelf profile monitoring. *Radar, Sonar & Navigation, IET*, *8*(7), 776–786. https://doi.org/10.1049/iet-rsn.2013.0053

Brook, E., & Nesbitt, I. (2023). I-165-M GPR field report 2019-2020 [Dataset]. *U.S. Antarctic Program (USAP) Data Center*. https://doi.org/10.15784/601669

Cassidy, W., Harvey, R., Schutt, J., Delisle, G., & Yanai, K. (1992). The meteorite collection sites of Antarctica. *Meteoritics*, *27*(5), 490–525. https://doi.org/10.1111/j.1945-5100.1992.tb01073.x

Chung, A., Parrenin, F., Mulvaney, R., Vittuari, L., Frezzotti, M., Zanutta, A., et al. (2025). Age, thinning and spatial origin of the beyond EPICA ice from a 2.5D ice flow model. *The Cryosphere*, *19*(10), 4125–4140. https://doi.org/10.5194/tc-19-4125-2025

Chung, A., Parrenin, F., Steinhage, D., Mulvaney, R., Martín, C., Cavitte, M. G. P., et al. (2023). Stagnant ice and age modelling in the Dome C region, Antarctica. *The Cryosphere*, *17*(8), 3461–3483. (Publisher: Copernicus GmbH). https://doi.org/10.5194/tc-17-3461-2023

Coleman, T. F., & Li, Y. (1996). An interior trust region approach for nonlinear minimization subject to bounds. *SIAM Journal on Optimization*, *6*(2), 418–445. https://doi.org/10.1137/0806023

Conway, H., & Campbell, S. (2017). Ground-based ice-penetrating radar profiles collected on the Allan Hills Blue ice region [Dataset]. *U.S. Antarctic Program (USAP) Data Center*. Retrieved from https://www.usap-dc.org/view/dataset/601005

Coren, F., Delisle, G., & Sterzai, P. (2003). Ice dynamics of the Allan Hills meteorite concentration sites revealed by satellite aperture radar interferometry. *Meteoritics & Planetary Science*, *38*(9), 1319–1330. https://doi.org/10.1111/j.1945-5100.2003.tb00316.x

Corr, H. F. J., Jenkins, A., Nicholls, K. W., & Doake, C. S. M. (2002). Precise measurement of changes in ice-shelf thickness by phase-sensitive radar to determine basal melt rates. *Geophysical Research Letters*, *29*(8), 73-1–74-4. https://doi.org/10.1029/2001GL014618

Dadic, R., Mullen, P. C., Schneebeli, M., Brandt, R. E., & Warren, S. G. (2013). Effects of bubbles, cracks, and volcanic tephra on the spectral albedo of bare ice near the Transantarctic Mountains: Implications for sea glaciers on Snowball Earth. *Journal of Geophysical Research: Earth Surface*, *118*(3), 1658–1676. https://doi.org/10.1002/jgrf.20098

Dadic, R., Schneebeli, M., Bertler, N. A. N., Schwikowski, M., & Matzl, M. (2015). Extreme snow metamorphism in the Allan Hills, Antarctica, as an analogue for glacial conditions with implications for stable isotope composition. *Journal of Glaciology*, *61*(230), 1171–1182. https://doi.org/10.3189/2015JoG15J027

Delisle, G., & Sievers, J. (1991). Sub-ice topography and meteorite finds near the Allan Hills and the Near Western Ice Field, Victoria Land, Antarctica. *Journal of Geophysical Research*, *96*(E1), 15577–15587. https://doi.org/10.1029/91JE01117

Drews, R., Eisen, O., Weikusat, I., Kipfstuhl, S., Lambrecht, A., Steinhage, D., et al. (2009). Layer disturbances and the radio-echo free zone in ice sheets. *The Cryosphere*, *3*(2), 195–203. https://doi.org/10.5194/tc-3-195-2009

Engl, H. W., & Grever, W. (1994). Using the L–curve for determiningoptimal regularization parameters. *Numerische Mathematik*, *69*(1), 25–31. https://doi.org/10.1007/s002110050078

EPICA community Members. (2004). Eight glacial cycles from an Antarctic ice core. *Nature*, *429*(6992), 623–628. https://doi.org/10.1038/nature02599

Ershadi, M. R., Drews, R., Martín, C., Eisen, O., Ritz, C., Corr, H., et al. (2022). Polarimetric radar reveals the spatial distribution of ice fabric at domes and divides in East Antarctica. *The Cryosphere*, *16*(5), 1719–1739. https://doi.org/10.5194/tc-16-1719-2022

Fireman, E. L., Rancitelli, L. A., & Kirsten, T. (1979). Terrestrial ages of four Allan Hills Meteorites: Consequences for Antarctic Ice. *Science*, *203*(4379), 453–455. https://doi.org/10.1126/science.203.4379.453

Franke, S., Gerber, T., Warren, C., Jansen, D., Eisen, O., & Dahl-Jensen, D. (2023). Investigating the radar response of englacial debris entrained basal ice units in East Antarctica using electromagnetic forward modeling. *IEEE Transactions on Geoscience and Remote Sensing*, *61*, 1–16. https://doi.org/10.1109/TGRS.2023.3277874

Fudge, T. J., Hills, B. H., Horlings, A. N., Holschuh, N., Christian, J. E., Davidge, L., et al. (2023). A site for deep ice coring at West Hercules Dome: Results from ground-based geophysics and modeling. *Journal of Glaciology*, *69*(275), 538–550. https://doi.org/10.1017/jog.2022.80

Fujita, S., Maeno, H., & Matsuoka, K. (2006). Radio-wave depolarization and scattering within ice sheets: A matrix-based model to link radar and ice-core measurements and its application. *Journal of Glaciology*, *52*(178), 407–424. https://doi.org/10.3189/172756506781828548

Grinsted, A., Moore, J., Spikes, V. B., & Sinisalo, A. (2003). Dating Antarctic blue ice areas using a novel ice flow model. *Geophysical Research Letters*, *30*(19). https://doi.org/10.1029/2003GL017957

Harvey, R. (2003). The origin and significance of Antarctic meteorites. *Geochemistry*, *63*(2), 93–147. https://doi.org/10.1078/0009-2819-00031

Higgins, J. A., Kurbatov, A. V., Spaulding, N. E., Brook, E., Introne, D. S., Chimiak, L. M., et al. (2015). Atmospheric composition 1 million years ago from blue ice in the Allan Hills, Antarctica. *Proceedings of the National Academy of Sciences*, *112*(22), 6887–6891. https://doi.org/10.1073/pnas.1420232112

Hills, B. H., Christianson, K., Hoffman, A. O., Fudge, T. J., Holschuh, N., Kahle, E. C., et al. (2022). Geophysics and thermodynamics at South Pole Lake indicate stability and a regionally thawed bed. *Geophysical Research Letters*, *49*(2), e2021GL096218. https://doi.org/10.1029/2021GL096218

Hills, B. H., Young, T. J., Lilien, D. A., Babcock, E., Bienert, N., Blankenship, D., et al. (2025). Radar polarimetry in glaciology: Theory, measurement techniques, and scientific applications for investigating the anisotropy of ice masses. *Reviews of Geophysics*, *63*(4), e2024RG000842. https://doi.org/10.1029/2024RG000842

Holschuh, N., Christianson, K., Dienstfrey, W., Hills, B., Hoffman, A. O., Paden, J., et al. (2026). Entrained debris records regrowth of the Greenland Ice Sheet after the last interglacial. *Nature Geoscience*, *19*(5), 573–580. https://doi.org/10.1038/s41561-026-01950-1

Holschuh, N., Parizek, B. R., Alley, R. B., & Anandakrishnan, S. (2017). Decoding ice sheet behavior using englacial layer slopes. *Geophysical Research Letters*, *44*(11), 5561–5570. https://doi.org/10.1002/2017GL073417

Hui, F., Ci, T., Cheng, X., Scambo, T. A., Liu, Y., Zhang, Y., et al. (2014). Mapping blue-ice areas in Antarctica using ETM+ and MODIS data. *Annals of Glaciology*, *55*(66), 129–137. https://doi.org/10.3189/2014AoG66A069

Jordan, T. M., Schroeder, D. M., Castelletti, D., Li, J., & Dall, J. (2019). A polarimetric coherence method to determine ice crystal orientation fabric from radar sounding: Application to the NEEM ice core region. *IEEE Transactions on Geoscience and Remote Sensing*, *57*(11), 8641–8657. (Conference Name: IEEE Transactions on Geoscience and Remote Sensing). https://doi.org/10.1109/TGRS.2019.2921980

Kehrl, L., Conway, H., Holschuh, N., Campbell, S., Kurbatov, A. V., & Spaulding, N. E. (2018). Evaluating the duration and continuity of potential climate records from the Allan Hills Blue Ice Area, East Antarctica. *Geophysical Research Letters*, *45*(9), 4096–4104. https://doi.org/10.1029/2018GL077511

Kingslake, J., Hindmarsh, R. C. A., Aðalgeirsdóttir, G., Conway, H., Corr, H. F. J., Gillet-Chaulet, F., et al. (2014). Full-depth englacial vertical ice sheet velocities measured using phase-sensitive radar. *Journal of Geophysical Research: Earth Surface*, *119*(12), 2604–2618. https://doi.org/10.1002/2014JF003275

Kingslake, J., Martín, C., Arthern, R. J., Corr, H. F. J., & King, E. C. (2016). Ice-flow reorganization in West Antarctica 2.5 kyr ago dated using radar-derived englacial flow velocities. *Geophysical Research Letters*, *43*(17), 9103–9112. https://doi.org/10.1002/2016GL070278

Kirkpatrick, L. R., Carter, A. J., Marks-Peterson, J., Shackleton, S., & Fudge, T. J. (2025). Three-dimensional multitrack electrical conductivity method for interpretation of complex ice core stratigraphy. *Journal of Glaciology*, *71*, e105. https://doi.org/10.1017/jog.2025.10081

Lilien, D. A., Steinhage, D., Taylor, D., Parrenin, F., Ritz, C., Mulvaney, R., et al. (2021). Brief communication: New radar constraints support presence of ice older than 1.5 Myr at Little Dome C. *The Cryosphere*, *15*(4), 1881–1888. https://doi.org/10.5194/tc-15-1881-2021

Lliboutry, L. (1979). A critical review of analytical approximate solutions for steady state velocities and temperatures in cold ice-sheets. *Z. Gletscherkde*, *15*, 135–148.

Lombardi, D., Gorodetskaya, I., Barruol, G., & Camelbeeck, T. (2019). Thermally induced icequakes detected on blue ice areas of the East Antarctic ice sheet. *Annals of Glaciology*, *60*(79), 45–56. https://doi.org/10.1017/aog.2019.26

MacGregor, J. A., Li, J., Paden, J. D., Catania, G. A., Clow, G. D., Fahnestock, M. A., et al. (2015). Radar attenuation and temperature within the Greenland Ice Sheet. *Journal of Geophysical Research: Earth Surface*, *120*(6), 983–1008. https://doi.org/10.1002/2014JF003418

Marks-Peterson, J., Shackleton, S., Higgins, J., Severinghaus, J., Yan, Y., Buizert, C., et al. (2026). Broadly stable atmospheric CO_2 and CH_4 levels over the past 3 million years. *Nature*, *651*(8106), 647–652. https://doi.org/10.1038/s41586-025-10032-y

Marsh, O. J., Fricker, H. A., Siegfried, M. R., Christianson, K., Nicholls, K. W., Corr, H. F. J., & Catania, G. (2016). High basal melting forming a channel at the grounding line of Ross Ice Shelf, Antarctica. *Geophysical Research Letters*, *43*(1), 250–255. https://doi.org/10.1002/2015GL066612

Meyer, C. R., & Creyts, T. T. (2017). Formation of ice eddies in subglacial mountain valleys. *Journal of Geophysical Research: Earth Surface*, *122*(9), 1574–1588. https://doi.org/10.1002/2017JF004329

Mutter, E. L., & Holschuh, N. (2025). Advancing interpretation of incoherent scattering in ice-penetrating radar data used for ice core site selection. *The Cryosphere*, *19*(8), 3159–3176. https://doi.org/10.5194/tc-19-3159-2025

Nicholls, K. W., Corr, H. F. J., Stewart, C. L., Lok, L. B., Brennan, P. V., & Vaughan, D. G. (2015). A ground-based radar for measuring vertical strain rates and time-varying basal melt rates in ice sheets and shelves. *Journal of Glaciology*, *61*(230), 1079–1087. https://doi.org/10.3189/2015JoG15J073

Parrenin, F., & Hindmarsh, R. (2007). Influence of a non-uniform velocity field on isochrone geometry along a steady flowline of an ice sheet. *Journal of Glaciology*, *53*(183), 612–622. https://doi.org/10.3189/002214307784409298

Pettit, E. C., Whorton, E. N., Waddington, E. D., & Sletten, R. S. (2014). Influence of debris-rich basal ice on flow of a polar glacier. *Journal of Glaciology*, *60*(223), 989–1006. https://doi.org/10.3189/2014JoG13J161

Raymond, C. F. (1983). Deformation in the vicinity of ice divides. *Journal of Glaciology*, *29*(103), 357–373. https://doi.org/10.3189/S0022143000030288

Scherer, P., Schultz, L., Neupert, U., Knauer, M., Neumann, S., Leya, I., et al. (1997). Allan Hills 88019: An Antarctic H-chondrite with a very long terrestrial age. *Meteoritics & Planetary Science*, *32*(6), 769–773. https://doi.org/10.1111/j.1945-5100.1997.tb01567.x

Schild, K. M., Vaňková, I., Sutherland, D. A., & Nicholls, K. (2024). Deriving iceberg ablation rates using an on-iceberg autonomous phase-sensitive radar (ApRES). *Annals of Glaciology*, *65*, e34. https://doi.org/10.1017/aog.2024.35

Schultz, J., Annexstad, L., & Delisle, G. (1990). Ice movement and mass balance at the Allan Hills Icefield. *Antarctic Journal of the United States*, *25*(5), 94–95.

Shackleton, S., Hishamunda, V., Davidge, L., Brook, E., Peterson, J. M., Carter, A., et al. (2025). Miocene and Pliocene ice and air from the Allan Hills blue ice area, East Antarctica. *Proceedings of the National Academy of Sciences*, *122*(44), e2502681122. https://doi.org/10.1073/pnas.2502681122

Shackleton, S., Hishamunda, V., Yan, Y., Carter, A., Morgan, J., Severinghaus, J., et al. (2026). Global ocean heat content over the past 3 million years. *Nature*, *651*(8106), 653–657. https://doi.org/10.1038/s41586-026-10116-3

Shaya, M., Manos, J.-M., Banerjee, A., Brook, E., Carter, A., Chalif, J., et al. (2026). GPS stake measurements of surface ice flow at the Allan Hills, Antarctica (2023-2025) [Dataset]. *U.S. Antarctic Program (USAP) Data Center*. https://doi.org/10.15784/602026

Shaya, M., Manos, J.-M., Li, A., Horlings, A., Conway, H., Banerjee, A., et al. (2026). Repeat ApRES survey of the Allan Hills, Antarctica (2022-2026) [Dataset]. *U.S. Antarctic Program (USAP) Data Center*. https://doi.org/10.15784/602075

Sinisalo, A., Grinsted, A., & Moore, J. (2004). Dynamics of the Scharffenbergbotnen blue-ice area, Dronning Maud Land, Antarctica. *Annals of Glaciology*, *39*, 417–422. https://doi.org/10.3189/172756404781814177

21699011, 2026, 11, Downloaded from https://agupubs.onlinelibrary.wiley.com/doi/10.1029/2026JF009592 by British Antarctic Survey, Wiley Online Library on [27/11/2026]. See the Terms and Conditions (https://onlinelibrary.wiley.com/terms-and-conditions) on Wiley Online Library for rules of use; OA articles are governed by the applicable Creative Commons License

Sinisalo, A., Moore, J. C., Van De Wal, R. S., Bintanja, R., & Jonsson, S. (2003). A 14 year mass-balance record of a blue-ice area in Antarctica. *Annals of Glaciology*, *37*, 213–218. https://doi.org/10.3189/172756403781816013

Spaulding, N. E., Higgins, J. A., Kurbatov, A. V., Bender, M. L., Arcone, S. A., Campbell, S., et al. (2013). Climate archives from 90 to 250 ka in horizontal and vertical ice cores from the Allan Hills Blue Ice Area, Antarctica. *Quaternary Research*, *80*(3), 562–574. (Publisher: Cambridge University Press). https://doi.org/10.1016/j.yqres.2013.07.004

Spaulding, N. E., Spikes, V. B., Hamilton, G. S., Mayewski, P. A., Dunbar, N. W., Harvey, R. P., et al. (2012). Ice motion and mass balance at the Allan Hills blue-ice area, Antarctica, with implications for paleoclimate reconstructions. *Journal of Glaciology*, *58*(208), 399–406. (Publisher: Cambridge University Press). https://doi.org/10.3189/2012JoG11J176

Summers, P. T., Schroeder, D. M., & Siegfried, M. R. (2021). Constraining ice sheet basal sliding and horizontal velocity profiles using a stationary phase sensitive radar sounder. In *2021 IEEE International Geoscience and Remote Sensing Symposium IGARSS* (pp. 5524–5527). (ISSN: 2153-7003). https://doi.org/10.1109/IGARSS47720.2021.9554535

The MathWorks, Inc. (2024). lsqnonlin [Computer software manual]. *(MATLAB Optimization Toolbox function, R2024a)*. Retrieved from https://www.mathworks.com/help/optim/ug/lsqnonlin.html

Tollenaar, V., Zekollari, H., Lhermitte, S., Tax, D. M., Debaille, V., Goderis, S., et al. (2022). Unexplored Antarctic meteorite collection sites revealed through machine learning. *Science Advances*, *8*(4), eabj8138. https://doi.org/10.1126/sciadv.abj8138

Vaňková, I., Nicholls, K. W., Corr, H. F. J., Makinson, K., & Brennan, P. V. (2020). Observations of tidal melt and vertical strain at the Filchner-Ronne Ice Shelf, Antarctica. *Journal of Geophysical Research: Earth Surface*, *125*(1), e2019JF005280. https://doi.org/10.1029/2019JF005280

Waddington, E. D., Neumann, T. A., Koutnik, M. R., Marshall, H.-P., & Morse, D. L. (2007). Inference of accumulation-rate patterns from deep layers in glaciers and ice sheets. *Journal of Glaciology*, *53*(183), 694–712. https://doi.org/10.3189/002214307784409351

Whillans, I. M., & Cassidy, W. A. (1983). Catch a falling star: Meteorites and old ice. *Science*, *222*(4619), 55–57. https://doi.org/10.1126/science.222.4619.55

Wild, C. T., Kachuck, S. B., Luckman, A., Alley, K. E., Sharp, M. A., Smith, H., et al. (2024). Rift propagation signals the last act of the Thwaites Eastern Ice Shelf despite low basal melt rates. *Journal of Glaciology*, *70*, e21. https://doi.org/10.1017/jog.2024.64

Winter, K., Woodward, J., Dunning, S. A., Turney, C. S. M., Fogwill, C. J., Hein, A. S., et al. (2016). Assessing the continuity of the blue ice climate record at Patriot Hills, Horseshoe Valley, West Antarctica. *Geophysical Research Letters*, *43*(5), 2019–2026. https://doi.org/10.1002/2015GL066476

Winter, K., Woodward, J., Ross, N., Dunning, S. A., Hein, A. S., Westoby, M. J., et al. (2019). Radar-detected englacial debris in the West Antarctic Ice Sheet. *Geophysical Research Letters*, *46*(17–18), 10454–10462. https://doi.org/10.1029/2019GL084012

Yan, S., Young, D. A., Blankenship, D. D., Fudge, T. J., Li, D., Lindzey, L., et al. (2026). Basal unit radar characteristics at the southern flank of Dome A, East Antarctica. *The Cryosphere*, *20*(1), 453–465. https://doi.org/10.5194/tc-20-453-2026

Yan, Y., Bender, M. L., Brook, E. J., Clifford, H. M., Kemeny, P. C., Kurbatov, A. V., et al. (2019). Two-million-year-old snapshots of atmospheric gases from Antarctic ice. *Nature*, *574*(7780), 663–666. https://doi.org/10.1038/s41586-019-1692-3

Young, D. A., Paden, J. D., Yan, S., Kerr, M. E., Singh, S., Vega González, A., et al. (2025). Coupled ice sheet structure and bedrock geology in the deep interior of East Antarctica: Results from Dome A and the South Pole Basin. *Geophysical Research Letters*, *52*(19), e2025GL115729. https://doi.org/10.1029/2025GL115729

Young, T. J., Martín, C., Christoffersen, P., Schroeder, D. M., Tulaczyk, S. M., & Dawson, E. J. (2021). Rapid and accurate polarimetric radar measurements of ice crystal fabric orientation at the Western Antarctic Ice Sheet (WAIS) Divide ice core site. *The Cryosphere*, *15*(8), 4117–4133. https://doi.org/10.5194/tc-15-4117-2021

Young, T. J., Schroeder, D. M., Christoffersen, P., Lok, L. B., Nicholls, K. W., Brennan, P. V., et al. (2018). Resolving the internal and basal geometry of ice masses using imaging phase-sensitive radar. *Journal of Glaciology*, *64*(246), 649–660. https://doi.org/10.1017/jog.2018.54

Young, T. J., Schroeder, D. M., Jordan, T. M., Christoffersen, P., Tulaczyk, S. M., Culberg, R., & Bienert, N. L. (2021). Inferring ice fabric from birefringence loss in airborne radargrams: Application to the Eastern Shear Margin of Thwaites Glacier, West Antarctica. *Journal of Geophysical Research: Earth Surface*, *126*(5), e2020JF006023. https://doi.org/10.1029/2020JF006023

Zeising, O., Gerber, T. A., Eisen, O., Ershadi, M. R., Stoll, N., Weikusat, I., & Humbert, A. (2023). Improved estimation of the bulk ice crystal fabric asymmetry from polarimetric phase co-registration. *The Cryosphere*, *17*(3), 1097–1105. https://doi.org/10.5194/tc-17-1097-2023

Zeising, O., Steinhage, D., Nicholls, K. W., Corr, H. F. J., Stewart, C. L., & Humbert, A. (2022). Basal melt of the southern Filchner Ice Shelf, Antarctica. *The Cryosphere*, *16*(4), 1469–1482. https://doi.org/10.5194/tc-16-1469-2022

Zekollari, H., Goderis, S., Debaille, V., van Ginneken, M., Gattacceca, J., Timothy Jull, A. J., et al. (2019). Unravelling the high-altitude Nansen blue ice field meteorite trap (East Antarctica) and implications for regional palaeo-conditions. *Geochimica et Cosmochimica Acta*, *248*, 289–310. https://doi.org/10.1016/j.gca.2018.12.035

Zwinger, T., Schäfer, M., Martín, C., & Moore, J. C. (2014). Influence of anisotropy on velocity and age distribution at Scharffenbergbotnen blue ice area. *The Cryosphere*, *8*(2), 607–621. https://doi.org/10.5194/tc-8-607-2014

21699011, 2026, 11, Downloaded from https://agupubs.onlinelibrary.wiley.com/doi/10.1029/2026JF009592 by British Antarctic Survey, Wiley Online Library on [27/11/2026]. See the Terms and Conditions (https://onlinelibrary.wiley.com/terms-and-conditions) on Wiley Online Library for rules of use; OA articles are governed by the applicable Creative Commons License